Precision measurements of $D_s^+ \to \eta e^+ \nu_e$ and $D_s^+ \to \eta' e^+ \nu_e$

M. Ablikim,[1] M. N. Achasov,[13,b] P. Adlarson,[75] R. Aliberti,[36] A. Amoroso,[74a,74c] M. R. An,[40] Q. An,[71,58] Y. Bai,[57] O. Bakina,[37] I. Balossino,[30a] Y. Ban,[47,g] V. Batozskaya,[1,45] K. Begzsuren,[33] N. Berger,[36] M. Berlowski,[45] M. Bertani,[29a] D. Bettoni,[30a] F. Bianchi,[74a,74c] E. Bianco,[74a,74c] J. Bloms,[68] A. Bortone,[74a,74c] I. Boyko,[37] R. A. Briere,[5] A. Brueggemann,[68] H. Cai,[76] X. Cai,[1,58] A. Calcaterra,[29a] G. F. Cao,[1,63] N. Cao,[1,63] S. A. Cetin,[62a] J. F. Chang,[1,58] T. T. Chang,[77] W. L. Chang,[1,63] G. R. Che,[44] G. Chelkov,[37,a] C. Chen,[44] Chao Chen,[55] G. Chen,[1] H. S. Chen,[1,63] M. L. Chen,[1,58,63] S. J. Chen,[43] S. M. Chen,[61] T. Chen,[1,63] X. R. Chen,[32,63] X. T. Chen,[1,63] Y. B. Chen,[1,58] Y. Q. Chen,[35] Z. J. Chen,[26,h] W. S. Cheng,[74c] S. K. Choi,[10] X. Chu,[44] G. Cibinetto,[30a] S. C. Coen,[4] F. Cossio,[74c] J. J. Cui,[50] H. L. Dai,[1,58] J. P. Dai,[79] A. Dbeyssi,[19] R. E. de Boer,[4] D. Dedovich,[37] Z. Y. Deng,[1] A. Denig,[36] I. Denysenko,[37] M. Destefanis,[74a,74c] F. De Mori,[74a,74c] B. Ding,[66,1] X. X. Ding,[47,g] Y. Ding,[41] Y. Ding,[35] J. Dong,[1,58] L. Y. Dong,[1,63] M. Y. Dong,[1,58,63] X. Dong,[76] S. X. Du,[81] Z. H. Duan,[43] P. Egorov,[37,a] Y. L. Fan,[76] J. Fang,[1,58] S. S. Fang,[1,63] W. X. Fang,[1] Y. Fang,[1] R. Farinelli,[30a] L. Fava,[74b,74c] F. Feldbauer,[4] G. Felici,[29a] C. Q. Feng,[71,58] J. H. Feng,[59] K Fischer,[69] M. Fritsch,[4] C. Fritzsch,[68] C. D. Fu,[1] J. L. Fu,[63] Y. W. Fu,[1] H. Gao,[63] Y. N. Gao,[47,g] Yang Gao,[71,58] S. Garbolino,[74c] I. Garzia,[30a,30b] P. T. Ge,[76] Z. W. Ge,[43] C. Geng,[59] E. M. Gersabeck,[67] A Gilman,[69] K. Goetzen,[14] L. Gong,[41] W. X. Gong,[1,58] W. Gradl,[36] S. Gramigna,[30a,30b] M. Greco,[74a,74c] M. H. Gu,[1,58] Y. T. Gu,[16] C. Y Guan,[1,63] Z. L. Guan,[23] A. Q. Guo,[32,63] L. B. Guo,[42] R. P. Guo,[49] Y. P. Guo,[12,f] A. Guskov,[37,a] X. T. H.,[1,63] T. T. Han,[50] W. Y. Han,[40] X. Q. Hao,[20] F. A. Harris,[65] K. K. He,[55] K. L. He,[1,63] F. H. H. Heinsius,[4] C. H. Heinz,[36] Y. K. Heng,[1,58,63] C. Herold,[60] T. Holtmann,[4] P. C. Hong,[12,f] G. Y. Hou,[1,63] Y. R. Hou,[63] Z. L. Hou,[1] H. M. Hu,[1,63] J. F. Hu,[56,i] T. Hu,[1,58,63] Y. Hu,[1] G. S. Huang,[71,58] K. X. Huang,[59] L. Q. Huang,[32,63] X. T. Huang,[50] Y. P. Huang,[1] T. Hussain,[73] N Hüsken,[28,36] W. Imoehl,[28] M. Irshad,[71,58] J. Jackson,[28] S. Jaeger,[4] S. Janchiv,[33] J. H. Jeong,[10] Q. Ji,[1] Q. P. Ji,[20] X. B. Ji,[1,63] X. L. Ji,[1,58] Y. Y. Ji,[50] Z. K. Jia,[71,58] P. C. Jiang,[47,g] S. S. Jiang,[40] T. J. Jiang,[17] X. S. Jiang,[1,58,63] Y. Jiang,[63] J. B. Jiao,[50] Z. Jiao,[24] S. Jin,[43] Y. Jin,[66] M. Q. Jing,[1,63] T. Johansson,[75] X. K.,[1] S. Kabana,[34] N. Kalantar-Nayestanaki,[64] X. L. Kang,[9] X. S. Kang,[41] R. Kappert,[64] M. Kavatsyuk,[64] B. C. Ke,[81] A. Khoukaz,[68] R. Kiuchi,[1] R. Kliemt,[14] L. Koch,[38] O. B. Kolcu,[62a] B. Kopf,[4] M. K. Kuessner,[4] A. Kupsc,[45,75] W. Kühn,[38] J. J. Lane,[67] J. S. Lange,[38] P. Larin,[19] A. Lavania,[27] L. Lavezzi,[74a,74c] T. T. Lei,[71,k] Z. H. Lei,[71,58] H. Leithoff,[36] M. Lellmann,[36] T. Lenz,[36] C. Li,[48] C. Li,[44] C. H. Li,[40] Cheng Li,[71,58] D. M. Li,[81] F. Li,[1,58] G. Li,[1] H. Li,[71,58] H. B. Li,[1,63] H. J. Li,[20] H. N. Li,[56,i] Hui Li,[44] J. R. Li,[61] J. S. Li,[59] J. W. Li,[50] Ke Li,[1] L. J Li,[1,63] L. K. Li,[1] Lei Li,[3] M. H. Li,[44] P. R. Li,[39,j,k] S. X. Li,[12] T. Li,[50] W. D. Li,[1,63] W. G. Li,[1] X. H. Li,[71,58] X. L. Li,[50] Xiaoyu Li,[1,63] Y. G. Li,[47,g] Z. J. Li,[59] Z. X. Li,[16] Z. Y. Li,[59] C. Liang,[43] H. Liang,[71,58] H. Liang,[35] H. Liang,[1,63] Y. F. Liang,[54] Y. T. Liang,[32,63] G. R. Liao,[15] L. Z. Liao,[50] J. Libby,[27] A. Limphirat,[60] D. X. Lin,[32,63] T. Lin,[1] B. J. Liu,[1] B. X. Liu,[76] C. Liu,[35] C. X. Liu,[1] D. Liu,[19,71] F. H. Liu,[53] Fang Liu,[1] Feng Liu,[6] G. M. Liu,[56,i] H. Liu,[39,j,k] H. B. Liu,[16] H. M. Liu,[1,63] Huanhuan Liu,[1] Huihui Liu,[22] J. B. Liu,[71,58] J. L. Liu,[72] J. Y. Liu,[1,63] K. Liu,[1] K. Y. Liu,[41] Ke Liu,[23] L. Liu,[71,58] L. C. Liu,[44] Lu Liu,[44] M. H. Liu,[12,f] P. L. Liu,[1] Q. Liu,[63] S. B. Liu,[71,58] T. Liu,[12,f] W. K. Liu,[44] W. M. Liu,[71,58] X. Liu,[39,j,k] Y. Liu,[39,j,k] Y. B. Liu,[44] Z. A. Liu,[1,58,63] Z. Q. Liu,[50] X. C. Lou,[1,58,63] F. X. Lu,[59] H. J. Lu,[24] J. G. Lu,[1,58] X. L. Lu,[1] Y. Lu,[7] Y. P. Lu,[1,58] Z. H. Lu,[1,63] C. L. Luo,[42] M. X. Luo,[80] T. Luo,[12,f] X. L. Luo,[1,58] X. R. Lyu,[63] Y. F. Lyu,[44] F. C. Ma,[41] H. L. Ma,[1] J. L. Ma,[1,63] L. L. Ma,[50] M. M. Ma,[1,63] Q. M. Ma,[1] R. Q. Ma,[1,63] R. T. Ma,[63] X. Y. Ma,[1,58] Y. Ma,[47,g] F. E. Maas,[19] M. Maggiora,[74a,74c] S. Maldaner,[4] S. Malde,[69] A. Mangoni,[29b] Y. J. Mao,[47,g] Z. P. Mao,[1] S. Marcello,[74a,74c] Z. X. Meng,[66] J. G. Messchendorp,[14,64] G. Mezzadri,[30a] H. Miao,[1,63] T. J. Min,[43] R. E. Mitchell,[28] X. H. Mo,[1,58,63] N. Yu. Muchnoi,[13,b] Y. Nefedov,[37] F. Nerling,[19,d] I. B. Nikolaev,[13,b] Z. Ning,[1,58] S. Nisar,[11,l] Y. Niu,[50] S. L. Olsen,[63] Q. Ouyang,[1,58,63] S. Pacetti,[29b,29c] X. Pan,[55] Y. Pan,[57] A. Pathak,[35] P. Patteri,[29a] Y. P. Pei,[71,58] M. Pelizaeus,[4] H. P. Peng,[71,58] K. Peters,[14,d] J. L. Ping,[42] R. G. Ping,[1,63] S. Plura,[36] S. Pogodin,[37] V. Prasad,[34] F. Z. Qi,[1] H. Qi,[71,58] H. R. Qi,[61] M. Qi,[43] T. Y. Qi,[12,f] S. Qian,[1,58] W. B. Qian,[63] C. F. Qiao,[63] J. J. Qin,[72] L. Q. Qin,[15] X. P. Qin,[12,f] X. S. Qin,[50] Z. H. Qin,[1,58] J. F. Qiu,[1] S. Q. Qu,[61] C. F. Redmer,[36] K. J. Ren,[40] A. Rivetti,[74c] V. Rodin,[64] M. Rolo,[74c] G. Rong,[1,63] Ch. Rosner,[19] S. N. Ruan,[44] N. Salone,[45] A. Sarantsev,[37,c] Y. Schelhaas,[36] K. Schoenning,[75] M. Scodeggio,[30a,30b] K. Y. Shan,[12,f] W. Shan,[25] X. Y. Shan,[71,58] J. F. Shangguan,[55] L. G. Shao,[1,63] M. Shao,[71,58] C. P. Shen,[12,f] H. F. Shen,[1,63] W. H. Shen,[63] X. Y. Shen,[1,63] B. A. Shi,[63] H. C. Shi,[71,58] J. L. Shi,[12] J. Y. Shi,[1] Q. Q. Shi,[55] R. S. Shi,[1,63] X. Shi,[1,58] J. J. Song,[20] T. Z. Song,[59] W. M. Song,[35,1] Y. J. Song,[12] Y. X. Song,[47,g] S. Sosio,[74a,74a] S. Spataro,[74a,74c] F. Stieler,[36] Y. J. Su,[63] G. B. Sun,[76] G. X. Sun,[1] H. Sun,[63] H. K. Sun,[1] J. F. Sun,[20] K. Sun,[61] L. Sun,[76] S. S. Sun,[1,63] T. Sun,[1,63] W. Y. Sun,[35] Y. Sun,[9] Y. J. Sun,[71,58] Y. Z. Sun,[1] Z. T. Sun,[50] Y. X. Tan,[71,58] C. J. Tang,[54] G. Y. Tang,[1] J. Tang,[59] Y. A. Tang,[76] L. Y Tao,[72] Q. T. Tao,[26,h] M. Tat,[69] J. X. Teng,[71,58] V. Thoren,[75] W. H. Tian,[52] W. H. Tian,[59] Z. F. Tian,[76] I. Uman,[62b] B. Wang,[1] B. L. Wang,[63] Bo Wang,[71,58] C. W. Wang,[43] D. Y. Wang,[47,g] F. Wang,[72] H. J. Wang,[39,j,k] H. P. Wang,[1,63] K. Wang,[1,58] L. L. Wang,[1] M. Wang,[50] Meng Wang,[1,63] S. Wang,[12,f] S. Wang,[39,j,k] T. Wang,[12,f] T. J. Wang,[44] W. Wang,[72] W. Wang,[59] W. H. Wang,[76] W. P. Wang,[71,58] X. Wang,[47,g] X. F. Wang,[39,j,k] X. J. Wang,[40] X. L. Wang,[12,f] Y. Wang,[61] Y. D. Wang,[46] Y. F. Wang,[1,58,63] Y. H. Wang,[48] Y. N. Wang,[46] Y. Q. Wang,[1] Yaqian Wang,[18,1] Yi Wang,[61] Z. Wang,[1,58] Z. L. Wang,[72] Z. Y. Wang,[1,63] Ziyi Wang,[63] D. Wei,[70] D. H. Wei,[15] F. Weidner,[68] S. P. Wen,[1] C. W. Wenzel,[4]

U. W. Wiedner,[4] G. Wilkinson,[69] M. Wolke,[75] L. Wollenberg,[4] C. Wu,[40] J. F. Wu,[1,63] L. H. Wu,[1] L. J. Wu,[1,63] X. Wu,[12,f] X. H. Wu,[35] Y. Wu,[71] Y. J Wu,[32] Z. Wu,[1,58] L. Xia,[71,58] X. M. Xian,[40] T. Xiang,[47,g] D. Xiao,[39,j,k] G. Y. Xiao,[43] H. Xiao,[12,f] S. Y. Xiao,[1] Y. L. Xiao,[12,f] Z. J. Xiao,[42] C. Xie,[43] X. H. Xie,[47,g] Y. Xie,[50] Y. G. Xie,[1,58] Y. H. Xie,[6] Z. P. Xie,[71,58] T. Y. Xing,[1,63] C. F. Xu,[1,63] C. J. Xu,[59] G. F. Xu,[1] H. Y. Xu,[66] Q. J. Xu,[17] Q. N. Xu,[31] W. Xu,[1,63] W. L. Xu,[66] X. P. Xu,[55] Y. C. Xu,[78] Z. P. Xu,[43] Z. S. Xu,[63] F. Yan,[12,f] L. Yan,[12,f] W. B. Yan,[71,58] W. C. Yan,[81] X. Q Yan,[1] H. J. Yang,[51,e] H. L. Yang,[35] H. X. Yang,[1] Tao Yang,[1] Y. Yang,[12,f] Y. F. Yang,[44] Y. X. Yang,[1,63] Yifan Yang,[1,63] Z. W. Yang,[39,j,k] M. Ye,[1,58] M. H. Ye,[8] J. H. Yin,[1] Z. Y. You,[59] B. X. Yu,[1,58,63] C. X. Yu,[44] G. Yu,[1,63] T. Yu,[72] X. D. Yu,[47,g] C. Z. Yuan,[1,63] L. Yuan,[2] S. C. Yuan,[1] X. Q. Yuan,[1] Y. Yuan,[1,63] Z. Y. Yuan,[59] C. X. Yue,[40] A. A. Zafar,[73] F. R. Zeng,[50] X. Zeng,[12,f] Y. Zeng,[26,h] Y. J. Zeng,[1,63] X. Y. Zhai,[35] Y. H. Zhan,[59] A. Q. Zhang,[1,63] B. L. Zhang,[1,63] B. X. Zhang,[1] D. H. Zhang,[44] G. Y. Zhang,[20] H. Zhang,[71] H. H. Zhang,[59] H. H. Zhang,[35] H. Q. Zhang,[1,58,63] H. Y. Zhang,[1,58] J. J. Zhang,[52] J. L. Zhang,[21] J. Q. Zhang,[42] J. W. Zhang,[1,58,63] J. X. Zhang,[39,j,k] J. Y. Zhang,[1] J. Z. Zhang,[1,63] Jianyu Zhang,[63] Jiawei Zhang,[1,63] L. M. Zhang,[61] L. Q. Zhang,[59] Lei Zhang,[43] P. Zhang,[1] Q. Y. Zhang,[40,81] Shuihan Zhang,[1,63] Shulei Zhang,[26,h] X. D. Zhang,[46] X. M. Zhang,[1] X. Y. Zhang,[55] X. Y. Zhang,[50] Y. Zhang,[72] Y. Zhang,[69] Y. T. Zhang,[81] Y. H. Zhang,[1,58] Yan Zhang,[71,58] Yao Zhang,[1] Z. H. Zhang,[1] Z. L. Zhang,[35] Z. Y. Zhang,[44] Z. Y. Zhang,[76] G. Zhao,[1] J. Zhao,[40] J. Y. Zhao,[1,63] J. Z. Zhao,[1,58] Lei Zhao,[71,58] Ling Zhao,[1] M. G. Zhao,[44] S. J. Zhao,[81] Y. B. Zhao,[1,58] Y. X. Zhao,[32,63] Z. G. Zhao,[71,58] A. Zhemchugov,[37,a] B. Zheng,[72] J. P. Zheng,[1,58] W. J. Zheng,[1,63] Y. H. Zheng,[63] B. Zhong,[42] X. Zhong,[59] H. Zhou,[50] L. P. Zhou,[1,63] X. Zhou,[76] X. K. Zhou,[6] X. R. Zhou,[71,58] X. Y. Zhou,[40] Y. Z. Zhou,[12,f] J. Zhu,[44] K. Zhu,[1] K. J. Zhu,[1,58,63] L. Zhu,[35] L. X. Zhu,[63] S. H. Zhu,[70] S. Q. Zhu,[43] T. J. Zhu,[12,f] W. J. Zhu,[12,f] Y. C. Zhu,[71,58] Z. A. Zhu,[1,63] J. H. Zou,[1] and J. Zu[71,58]

(BESIII Collaboration)

[1]*Institute of High Energy Physics, Beijing 100049, People's Republic of China*
[2]*Beihang University, Beijing 100191, People's Republic of China*
[3]*Beijing Institute of Petrochemical Technology, Beijing 102617, People's Republic of China*
[4]*Bochum Ruhr-University, D-44780 Bochum, Germany*
[5]*Carnegie Mellon University, Pittsburgh, Pennsylvania 15213, USA*
[6]*Central China Normal University, Wuhan 430079, People's Republic of China*
[7]*Central South University, Changsha 410083, People's Republic of China*
[8]*China Center of Advanced Science and Technology, Beijing 100190, People's Republic of China*
[9]*China University of Geosciences, Wuhan 430074, People's Republic of China*
[10]*Chung-Ang University, Seoul, 06974, Republic of Korea*
[11]*COMSATS University Islamabad, Lahore Campus,*
Defence Road, Off Raiwind Road, 54000 Lahore, Pakistan
[12]*Fudan University, Shanghai 200433, People's Republic of China*
[13]*G.I. Budker Institute of Nuclear Physics SB RAS (BINP), Novosibirsk 630090, Russia*
[14]*GSI Helmholtzcentre for Heavy Ion Research GmbH, D-64291 Darmstadt, Germany*
[15]*Guangxi Normal University, Guilin 541004, People's Republic of China*
[16]*Guangxi University, Nanning 530004, People's Republic of China*
[17]*Hangzhou Normal University, Hangzhou 310036, People's Republic of China*
[18]*Hebei University, Baoding 071002, People's Republic of China*
[19]*Helmholtz Institute Mainz, Staudinger Weg 18, D-55099 Mainz, Germany*
[20]*Henan Normal University, Xinxiang 453007, People's Republic of China*
[21]*Henan University, Kaifeng 475004, People's Republic of China*
[22]*Henan University of Science and Technology, Luoyang 471003, People's Republic of China*
[23]*Henan University of Technology, Zhengzhou 450001, People's Republic of China*
[24]*Huangshan College, Huangshan 245000, People's Republic of China*
[25]*Hunan Normal University, Changsha 410081, People's Republic of China*
[26]*Hunan University, Changsha 410082, People's Republic of China*
[27]*Indian Institute of Technology Madras, Chennai 600036, India*
[28]*Indiana University, Bloomington, Indiana 47405, USA*
[29a]*INFN Laboratori Nazionali di Frascati, I-00044, Frascati, Italy*
[29b]*INFN Sezione di Perugia, I-06100, Perugia, Italy*
[29c]*University of Perugia, I-06100, Perugia, Italy*
[30a]*INFN Sezione di Ferrara, I-44122, Ferrara, Italy*
[30b]*University of Ferrara, I-44122, Ferrara, Italy*
[31]*Inner Mongolia University, Hohhot 010021, People's Republic of China*
[32]*Institute of Modern Physics, Lanzhou 730000, People's Republic of China*
[33]*Institute of Physics and Technology, Peace Avenue 54B, Ulaanbaatar 13330, Mongolia*

[34]*Instituto de Alta Investigación, Universidad de Tarapacá, Casilla 7D, Arica, Chile*
[35]*Jilin University, Changchun 130012, People's Republic of China*
[36]*Johannes Gutenberg University of Mainz, Johann-Joachim-Becher-Weg 45, D-55099 Mainz, Germany*
[37]*Joint Institute for Nuclear Research, 141980 Dubna, Moscow region, Russia*
[38]*Justus-Liebig-Universitaet Giessen, II. Physikalisches Institut,*
Heinrich-Buff-Ring 16, D-35392 Giessen, Germany
[39]*Lanzhou University, Lanzhou 730000, People's Republic of China*
[40]*Liaoning Normal University, Dalian 116029, People's Republic of China*
[41]*Liaoning University, Shenyang 110036, People's Republic of China*
[42]*Nanjing Normal University, Nanjing 210023, People's Republic of China*
[43]*Nanjing University, Nanjing 210093, People's Republic of China*
[44]*Nankai University, Tianjin 300071, People's Republic of China*
[45]*National Centre for Nuclear Research, Warsaw 02-093, Poland*
[46]*North China Electric Power University, Beijing 102206, People's Republic of China*
[47]*Peking University, Beijing 100871, People's Republic of China*
[48]*Qufu Normal University, Qufu 273165, People's Republic of China*
[49]*Shandong Normal University, Jinan 250014, People's Republic of China*
[50]*Shandong University, Jinan 250100, People's Republic of China*
[51]*Shanghai Jiao Tong University, Shanghai 200240, People's Republic of China*
[52]*Shanxi Normal University, Linfen 041004, People's Republic of China*
[53]*Shanxi University, Taiyuan 030006, People's Republic of China*
[54]*Sichuan University, Chengdu 610064, People's Republic of China*
[55]*Soochow University, Suzhou 215006, People's Republic of China*
[56]*South China Normal University, Guangzhou 510006, People's Republic of China*
[57]*Southeast University, Nanjing 211100, People's Republic of China*
[58]*State Key Laboratory of Particle Detection and Electronics,*
Beijing 100049, Hefei 230026, People's Republic of China
[59]*Sun Yat-Sen University, Guangzhou 510275, People's Republic of China*
[60]*Suranaree University of Technology, University Avenue 111, Nakhon Ratchasima 30000, Thailand*
[61]*Tsinghua University, Beijing 100084, People's Republic of China*
[62a]*Turkish Accelerator Center Particle Factory Group, Istinye University, 34010, Istanbul, Turkey*
[62b]*Near East University, Nicosia, North Cyprus, 99138, Mersin 10, Turkey*
[63]*University of Chinese Academy of Sciences, Beijing 100049, People's Republic of China*
[64]*University of Groningen, NL-9747 AA Groningen, The Netherlands*
[65]*University of Hawaii, Honolulu, Hawaii 96822, USA*
[66]*University of Jinan, Jinan 250022, People's Republic of China*
[67]*University of Manchester, Oxford Road, Manchester, M13 9PL, United Kingdom*
[68]*University of Muenster, Wilhelm-Klemm-Strasse 9, 48149 Muenster, Germany*
[69]*University of Oxford, Keble Road, Oxford OX13RH, United Kingdom*
[70]*University of Science and Technology Liaoning, Anshan 114051, People's Republic of China*
[71]*University of Science and Technology of China, Hefei 230026, People's Republic of China*
[72]*University of South China, Hengyang 421001, People's Republic of China*
[73]*University of the Punjab, Lahore-54590, Pakistan*
[74a]*University of Turin and INFN, University of Turin, I-10125, Turin, Italy*
[74b]*University of Eastern Piedmont, I-15121, Alessandria, Italy*
[74c]*INFN, I-10125, Turin, Italy*
[75]*Uppsala University, Box 516, SE-75120 Uppsala, Sweden*
[76]*Wuhan University, Wuhan 430072, People's Republic of China*
[77]*Xinyang Normal University, Xinyang 464000, People's Republic of China*
[78]*Yantai University, Yantai 264005, People's Republic of China*
[79]*Yunnan University, Kunming 650500, People's Republic of China*
[80]*Zhejiang University, Hangzhou 310027, People's Republic of China*
[81]*Zhengzhou University, Zhengzhou 450001, People's Republic of China*

[a]Also at the Moscow Institute of Physics and Technology, Moscow 141700, Russia.
[b]Also at the Novosibirsk State University, Novosibirsk, 630090, Russia.
[c]Also at the NRC "Kurchatov Institute," PNPI, 188300, Gatchina, Russia.
[d]Also at Goethe University Frankfurt, 60323 Frankfurt am Main, Germany.
[e]Also at Key Laboratory for Particle Physics, Astrophysics and Cosmology, Ministry of Education, Shanghai Key Laboratory for Particle Physics and Cosmology, Institute of Nuclear and Particle Physics, Shanghai 200240, People's Republic of China.

Precision measurements of the semileptonic decays $D_s^+ \to \eta e^+ \nu_e$ and $D_s^+ \to \eta' e^+ \nu_e$ are performed with 7.33 fb^{-1} of e^+e^- collision data collected at center-of-mass energies between 4.128 and 4.226 GeV with the BESIII detector. The branching fractions obtained are $\mathcal{B}(D_s^+ \to \eta e^+ \nu_e) = (2.255 \pm 0.039_{\text{stat}} \pm 0.051_{\text{syst}})\%$ and $\mathcal{B}(D_s^+ \to \eta' e^+ \nu_e) = (0.810 \pm 0.038_{\text{stat}} \pm 0.024_{\text{syst}})\%$. Combining these results with the $\mathcal{B}(D^+ \to \eta e^+ \nu_e)$ and $\mathcal{B}(D^+ \to \eta' e^+ \nu_e)$ obtained from previous BESIII measurements, the $\eta - \eta'$ mixing angle in the quark flavor basis is determined to be $\phi_P = (40.0 \pm 2.0_{\text{stat}} \pm 0.6_{\text{syst}})°$. Moreover, from the fits to the partial decay rates of $D_s^+ \to \eta e^+ \nu_e$ and $D_s^+ \to \eta' e^+ \nu_e$, the products of the hadronic transition form factors $f_+^{\eta^{(\prime)}}(0)$ and the modulus of the $c \to s$ Cabibbo-Kobayashi-Maskawa matrix element $|V_{cs}|$ are determined by using different hadronic transition form factor parametrizations. Based on the two-parameter series expansion, the products $f_+^{\eta}(0)|V_{cs}| = 0.4519 \pm 0.0071_{\text{stat}} \pm 0.0065_{\text{syst}}$ and $f_+^{\eta'}(0)|V_{cs}| = 0.525 \pm 0.024_{\text{stat}} \pm 0.009_{\text{syst}}$ are extracted. All results determined in this work supersede those measured in the previous BESIII analyses based on the 3.19 fb^{-1} subsample of data at 4.178 GeV.

DOI: 10.1103/PhysRevD.108.092003

I. INTRODUCTION

Experimental studies of the semileptonic decays of charmed mesons are important inputs to further understanding of the weak and strong interactions in the charm sector [1]. By analyzing their decay dynamics, one can extract the product of the modulus of the Cabibbo-Kobayashi-Maskawa (CKM) matrix element $|V_{cs(d)}|$ and the hadronic transition form factor, offering insights into charm physics. Taking $D_s^+ \to \eta^{(\prime)} e^+ \nu_e$ as an example, the hadronic transition form factors at zero-momentum transfer $f_+^{\eta^{(\prime)}}(0)$ [2–12] can be calculated via several theoretical approaches, e.g., lattice quantum chromodynamics (LQCD) [2], QCD light-cone sum rules (LCSR) [3–6], covariant light-front quark model (LFQM) [7,8],

[f] Also at Key Laboratory of Nuclear Physics and Ion-beam Application (MOE) and Institute of Modern Physics, Fudan University, Shanghai 200443, People's Republic of China.

[g] Also at State Key Laboratory of Nuclear Physics and Technology, Peking University, Beijing 100871, People's Republic of China.

[h] Also at School of Physics and Electronics, Hunan University, Changsha 410082, China.

[i] Also at Guangdong Provincial Key Laboratory of Nuclear Science, Institute of Quantum Matter, South China Normal University, Guangzhou 510006, China.

[j] Also at Frontiers Science Center for Rare Isotopes, Lanzhou University, Lanzhou 730000, People's Republic of China.

[k] Also at Lanzhou Center for Theoretical Physics, Lanzhou University, Lanzhou 730000, People's Republic of China.

[l] Also at the Department of Mathematical Sciences, IBA, Karachi 75270, Pakistan.

constituent quark model (CQM) [9], covariant confined quark model (CCQM) [10,11], and QCD sum rules (QCDSR) [12]. The predicted values for $f_+^{\eta}(0)$ and $f_+^{\eta'}(0)$ are summarized in Table I. Using the value of $|V_{cs}|$ provided by the CKMfitter group [13], the hadronic transition form factors can be extracted, resulting in a stringent test of the theoretical predictions. Alternatively, assuming a $f_+^{\eta^{(\prime)}}(0)$ value predicted by theory leads to $|V_{cs}|$, which is important for the test of CKM matrix unitarity.

In addition, the $\eta - \eta'$ mixing angle in the quark flavor basis, ϕ_P, can be related to the branching fractions of the semileptonic D^+ and D_s^+ decays, via $\cot^4 \phi_P = \frac{\Gamma_{D_s^+ \to \eta' e^+ \nu_e}/\Gamma_{D_s^+ \to \eta e^+ \nu_e}}{\Gamma_{D^+ \to \eta' e^+ \nu_e}/\Gamma_{D^+ \to \eta e^+ \nu_e}}$ [14]. In this double ratio, both D^+ and D_s^+ differences as well as the gluonium component in the η' cancel [14]. Compared with other extractions [15,16], this mixing angle can give information on the gluonium component to η' state, improving our understanding of nonperturbative QCD dynamics, which is being actively explored with LQCD calculations [17,18].

Previously, the branching fractions of $D_s^+ \to \eta e^+ \nu_e$ and $D_s^+ \to \eta' e^+ \nu_e$ were measured by CLEO-c [19–21] and BESIII [22,23]. Benefitting from the large data sample, BESIII reported measurements of the dynamics of these two decays, using 3.19 fb^{-1} of e^+e^- collision data taken at the center-of-mass energy $E_{\text{CM}} = 4.178$ GeV [23]. This paper reports the updated measurements of the $D_s^+ \to \eta^{(\prime)} e^+ \nu_e$ decay branching fractions and dynamics using 7.33 fb^{-1} of e^+e^- collision data collected by the BESIII detector at $E_{\text{CM}} = 4.128$, 4.157, 4.178, 4.189, 4.199, 4.209, 4.219, and 4.226 GeV. The integrated luminosities [24] for these subsamples are 0.402, 0.409, 3.189, 0.570, 0.526, 0.572, 0.569, and 1.092 fb^{-1}, respectively, with an uncertainty of 1%. Charge conjugated modes are implied throughout this paper.

TABLE I. Theoretical predictions of the hadronic transition form factors at zero-momentum transfer $f_+^{\eta^{(\prime)}}(0)$.

	$f_+^{\eta}(0)$	$f_+^{\eta'}(0)$
LQCD(I) [2]	0.542 ± 0.013	0.404 ± 0.025
LQCD(II) [2]	0.564 ± 0.011	0.437 ± 0.018
LCSR [3]	$0.476^{+0.040}_{-0.036}$	$0.544^{+0.046}_{-0.042}$
LCSR [4]	$0.495^{+0.030}_{-0.029}$	$0.558^{+0.047}_{-0.045}$
LCSR [5]	0.432 ± 0.033	0.520 ± 0.080
LCSR [6]	0.45 ± 0.14	0.55 ± 0.18
LFQM(I) [7]	0.50	0.62
LFQM(II) [7]	0.48	0.60
LFQM [8]	0.76	$\cdots$
CQM [9]	0.78	0.78
CCQM [10]	0.49 ± 0.07	0.59 ± 0.09
CCQM [11]	0.78 ± 0.12	0.73 ± 0.11
QCDSR [12]	0.50 ± 0.04	$\cdots$

II. BESIII DETECTOR AND MONTE CARLO SIMULATIONS

The BESIII detector [25] records symmetric e^+e^- collisions provided by the BEPCII storage ring [26] in the center-of-mass energy range from 2.0 to 4.95 GeV, with a peak luminosity of 1×10^{33} cm^{-2} s^{-1} achieved at $\sqrt{s} = 3.77$ GeV. BESIII has collected large data samples in this energy region [27,28]. The cylindrical core of the BESIII detector covers 93% of the full solid angle and consists of a helium-based multilayer drift chamber (MDC), a plastic scintillator time-of-flight system (TOF), and a CsI(Tl) electromagnetic calorimeter (EMC), which are all enclosed in a superconducting solenoidal magnet providing a 1.0 T magnetic field. The solenoid is supported by an octagonal flux-return yoke with resistive plate counter muon identification modules interleaved with steel. The charged-particle momentum resolution at 1 GeV/c is 0.5%, and the dE/dx resolution is 6% for electrons from Bhabha scattering. The EMC measures photon energies with a resolution of 2.5% (5%) at 1 GeV in the barrel (end cap) region. The time resolution in the TOF barrel region is 68 ps, while that in the end cap region was 110 ps. The end cap TOF system was upgraded in 2015 using multi-gap resistive plate chamber technology, providing a time resolution of 60 ps [29]. Approximately 83% of the data used here was collected after this upgrade.

Simulated samples produced with a GEANT4-based [30] Monte Carlo (MC) package, which includes the geometric description [31] of the BESIII detector and the detector response, are used to determine detection efficiencies and to estimate backgrounds. The simulation models the beam energy spread and initial state radiation (ISR) in the e^+e^- annihilations with the generator KKMC [32]. The input cross section of $e^+e^- \to D_s^\pm D_s^{*\mp}$ is taken from Ref. [33]. The ISR production of vector charmonium(like) states and the continuum processes are incorporated in KKMC [32]. In the simulation, the production of open-charm final states directly via e^+e^- annihilations is modeled with the generator CONEXC [34], and their subsequent decays are modeled by EvtGen [35] with known branching fractions from the Particle Data Group [36]. The remaining unknown charmonium decays are modeled with LUNDCHARM [37]. Final state radiation from charged final-state particles is incorporated using the PHOTOS package [38].

III. ANALYSIS METHOD

A double-tag (DT) measurement strategy, analogous to what is used in Refs. [23,39,40], is employed. At E_{CM} between 4.128 and 4.226 GeV, D_s mesons are produced mainly from the process $e^+e^- \to D_s^{*\pm}[\to \gamma(\pi^0)D_s^\pm]D_s^\mp$. First, a D_s^- meson is fully reconstructed in one of several hadronic decay modes, discussed in Sec. IV; this is referred to as a single-tag (ST) candidate. This includes the D_s directly from e^+e^- annihilations and the D_s from D_s^* decays. Then, the signal decay of the D_s^+ meson and the transition $\gamma(\pi^0)$ from the $D_s^{*\pm}$ decay are reconstructed from the remaining particles in the event; these are the DT candidates. The branching fraction of the semileptonic decay is determined by

$$\mathcal{B}_{SL} = \frac{N_{DT}}{N_{ST} \cdot \bar{\epsilon}_{\gamma(\pi^0)SL} \cdot \mathcal{B}_{sub}}. \qquad (1)$$

Here, $N_{DT} = \sum_{ij} N_{DT}^{ij}$ and $N_{ST} = \sum_{ij} N_{ST}^{ij}$ are the total DT and ST yields in data summing over tag mode i and dataset j; $\bar{\epsilon}_{\gamma(\pi^0)SL}$ is the efficiency of detecting the transition $\gamma(\pi^0)$ and the semileptonic decay in the presence of the ST D_s^- candidate, weighted by the ST yields in data. It is calculated by $\sum_{ij} [(N_{ST}^{ij}/N_{ST}) \cdot (\epsilon_{DT}^{ij}/\epsilon_{ST}^{ij})]$, where ϵ_{DT}^{ij} and ϵ_{ST}^{ij} are the detection efficiencies of the DT and ST candidates, respectively. The efficiencies do not include the branching fractions of $\eta^{(\prime)}$ [13]. The quantity $\mathcal{B}_{sub}$ is the product of the branching fractions of the relevant intermediate decays.

IV. SINGLE-TAG EVENT SELECTION

The ST D_s^- candidates are reconstructed from the fourteen hadronic decay modes $D_s^- \to K^+K^-\pi^-$, $K^-\pi^+\pi^-$, $\pi^+\pi^-\pi^-$, $K^+K^-\pi^-\pi^0$, $\eta'_{\gamma\rho^0}\pi^-$, $\eta_{\gamma\gamma}\rho^-$, $K_S^0K^-\pi^+\pi^-$, $K_S^0K^+\pi^-\pi^-$, $\eta_{\gamma\gamma}\pi^-$, $K_S^0K_S^0\pi^-$, $\eta_{\pi^0\pi^+\pi^-}\pi^-$, $\eta'_{\eta_{\gamma\gamma}\pi^+\pi^-}\pi^-$, $K_S^0K^-\pi^0$, and $K_S^0K^-$, where the subscripts of η and η' represent the decay modes used to reconstruct these mesons. Throughout this paper, ρ denotes $\rho(770)$.

The selection criteria of $K^\pm$, $\pi^\pm$, K_S^0, γ, π^0, and η are the same as those used in previous works [23,41,42].

All charged tracks must be within a polar angle range $|\cos\theta| < 0.93$. Except for those from K_S^0 decays, they are required to satisfy $|V_{xy}| < 1$ cm and $|V_z| < 10$ cm. Here, θ is the polar angle with respect to the MDC axis, and $|V_{xy}|$ and $|V_z|$ are the distances of the closest approach in the transverse plane and along the MDC axis, respectively. The particle identification (PID) of the charged particles is performed with the combined dE/dx and TOF information. The combined likelihoods ($\mathcal{L}$) under the pion and kaon hypotheses are obtained. Kaon and pion candidates are required to satisfy $\mathcal{L}_K > \mathcal{L}_\pi$ and $\mathcal{L}_\pi > \mathcal{L}_K$, respectively.

Each K_S^0 candidate is reconstructed from two oppositely charged tracks satisfying $|V_z| < 20$ cm. The two charged tracks are assigned as $\pi^+\pi^-$ without imposing PID criteria. They are constrained to originate from a common vertex and are required to have an invariant mass within $|M_{\pi^+\pi^-} - m_{K_S^0}| < 12$ MeV/c^2, where $m_{K_S^0}$ is the K_S^0 nominal mass [13] and 12 MeV/c^2 corresponds to about three times the fitted resolution around the K_S^0 nominal mass. The decay length of the K_S^0 candidate is required to be greater than twice the vertex resolution away from the interaction point.

The π^0 and η mesons are reconstructed from photon pairs. Photon candidates are identified as isolated showers in the EMC. The deposited energy of each shower must be more than 25 MeV in the barrel region ($|\cos\theta| < 0.80$) and more than 50 MeV in the end cap region ($0.86 < |\cos\theta| < 0.92$). The different energy thresholds for the barrel and end cap regions are due to different energy resolutions. To exclude showers that originate from charged tracks, we require the angle subtended by the EMC shower and the position of the closest charged track at the EMC must be greater than $10°$ as measured from the IP. The difference between the EMC time and the event start time, which is the interval of the trigger start time to the real collision time [43], is required to be within (0, 700) ns to suppress electronic noise and showers unrelated to the event. To form π^0 and η candidates, we require the invariant masses of the selected photon pairs, $M_{\gamma\gamma}$, to be within the intervals (0.115, 0.150) and (0.500, 0.570) GeV/c^2, respectively. To improve momentum resolution and suppress background, a kinematic fit is imposed on the selected photon pairs by constraining their invariant mass to the nominal π^0 or η mass [13].

The ρ^0 and ρ^- candidates are reconstructed from the $\pi^+\pi^-$ and $\pi^-\pi^0$ combinations with invariant masses within the interval (0.570, 0.970) GeV/c^2.

For the tag modes $D_s^- \to \eta_{\pi^0\pi^+\pi^-}\pi^-$ and $\eta_{\pi^0\pi^+\pi^-}\rho^-$, the $\pi^0\pi^+\pi^-$ decay mode is also used to form η candidates and the invariant mass, $M_{\pi^0\pi^+\pi^-}$, is required to be within the interval (0.530, 0.570) GeV/c^2. To form η' candidates, two decay modes $\eta_{\gamma\gamma}\pi^+\pi^-$ and $\gamma\rho^0$ are used; their invariant masses are required to be within the intervals (0.946, 0.970) GeV/c^2 and (0.940, 0.976) GeV/c^2, respectively.

TABLE II. The M_{BC} requirements for various energy points.

E_{CM} (GeV)	M_{BC} (GeV/c^2)
4.128	[2.010, 2.061]
4.157	[2.010, 2.070]
4.178	[2.010, 2.073]
4.189	[2.010, 2.076]
4.199	[2.010, 2.079]
4.209	[2.010, 2.082]
4.219	[2.010, 2.085]
4.226	[2.010, 2.088]

The difference in the invariant mass requirements for the $\eta_{\gamma\gamma}\pi^+\pi^-$ and $\gamma\rho^0$ decay modes is mainly due to different mass resolutions. In addition, the minimum energy of the γ from $\eta' \to \gamma\rho^0$ decays must be greater than 0.1 GeV.

The momentum of any pion, which does not originate from a K_S^0, η, or η' decay, is required to be greater than 0.1 GeV/c to reject the soft pions from D^{*+} decays. For the tag mode $D_s^- \to \pi^+\pi^-h^-$ ($h = K$ or π), the peaking background from $D_s^- \to K_S^0(\to \pi^+\pi^-)h^-$ is rejected by requiring the invariant mass of any $\pi^+\pi^-$ combination at least 30 MeV/c^2 away from the nominal K_S^0 mass [13].

To suppress non-$D_s^\pm D_s^{*\mp}$ events, the beam-constrained mass of the ST D_s^- candidate

$$M_{BC} \equiv \sqrt{E_{CM}^2/4c^4 - |\vec{p}_{tag}|^2/c^2} \qquad (2)$$

is required to be within the intervals shown in Table II, where $\vec{p}_{tag}$ is the momentum of the ST D_s^- candidate in the rest frame of the e^+e^- initial state. This requirement retains most of the D_s^- and D_s^+ mesons from $e^+e^- \to D_s^{*\mp}D_s^\pm$.

If there are multiple candidates for any tag mode, for a given ST D_s charge, in one event, the candidate with the D_s^- recoil mass

$$M_{rec} \equiv \sqrt{\left(E_{CM} - \sqrt{|\vec{p}_{tag}|^2c^2 + m_{D_s^-}^2c^4}\right)^2/c^4 - |\vec{p}_{tag}|^2/c^2} \qquad (3)$$

closest to the nominal D_s^{*+} mass [13] is kept. Here, $m_{D_s^-}$ is the nominal D_s^- mass [13]. The probability of the best candidate selection for individual tag modes ranges in (82–99)%. Figure 1 shows the invariant mass (M_{tag}) spectra of the accepted ST candidates for the 14 tag modes. For each tag mode, the ST yield is obtained by a fit to the corresponding M_{tag} spectrum. The signal is described by the simulated shape for events with the angle between the reconstructed and generated four-momentum less than $15°$, convolved with a Gaussian function representing the difference in resolution between data and simulation. For the tag mode $D_s^- \to K_S^0 K^-$, the peaking background from $D^- \to K_S^0 \pi^-$ is described by the simulated shape convolved

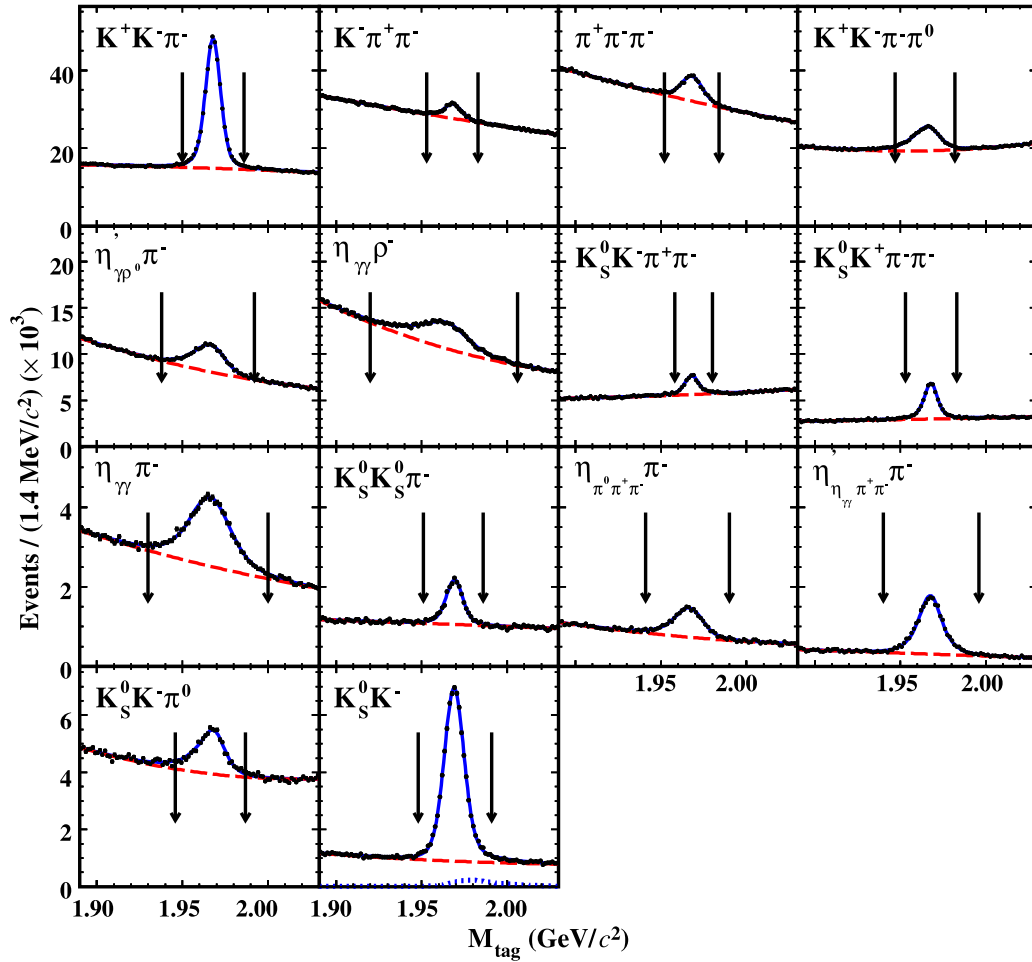FIG. 1. Fits to the M_{tag} distributions of the accepted ST candidates from the data sample with all datasets. Points with error bars are data. The blue solid curves are the total fit results. The red dashed curves are the fitted backgrounds. The blue dotted curve in the $K_S^0 K^-$ mode is the $D^- \to K_S^0 \pi^-$ component. In each subfigure, the pair of arrows denotes the signal regions.

with the same Gaussian function used in the signal shape and its yield is left as a free parameter. The non-peaking background is modeled by a second-order Chebychev polynomial, which has been validated using the inclusive simulation sample. The fit results for the data sample combined from all energy points are shown in Fig. 1. The candidates in the signal regions, marked with black arrows in each sub-figure, are kept for further analyses. The background contributions from $e^+e^- \to (\gamma_{\text{ISR}})D_s^+ D_s^-$, whose contribution is (0.7–1.1)% in the fitted ST yields for 14 tag modes based on simulation, are subtracted in this analysis. The resulting ST yields (N_{ST}) for the different tag modes in data and the corresponding ST efficiencies (ϵ_{ST}) are summarized in the second and third columns of Table III, respectively.

V. DOUBLE-TAG EVENT SELECTION

The transition photon or π^0 and the semileptonic D_s^+ decay candidate are selected from the particles remaining after ST reconstruction. The photon or π^0 providing the lowest energy difference, ΔE, is selected. Here, $\Delta E = E_{\text{CM}} - E_{\text{tag}} - E^{\text{rec}}_{\gamma(\pi^0)D_s^-} - E_{\gamma(\pi^0)}$, where the recoil energy is calculated from the momenta of $\gamma(\pi^0)$ and D_s^- tag as $E^{\text{rec}}_{\gamma(\pi^0)D_s^-} = \sqrt{|-\vec{p}_{\gamma(\pi^0)} - \vec{p}_{\text{tag}}|^2 c^2 + m_{D_s^+}^2 c^4}$. The signal candidates are examined using the kinematic variable $M^2_{\text{miss}} \equiv (E_{\text{CM}} - \sum_i E_i)^2/c^4 - |\sum_i \vec{p}_i|^2/c^2$, where E_i and $\vec{p}_i$, with $i = (\text{tag}, \gamma(\pi^0), e$ or $\eta^{(\prime)})$, are the energies and momenta of particle i. To improve the M^2_{miss} resolution, all the selected candidate tracks in the tag side, transition $\gamma(\pi^0)$, and $\eta^{(\prime)}e^+$ of the signal side, plus the missing neutrino, are subjected to a kinematic fit with a net three constraints: seven are applied and the neutrino four-vector is determined. The fit requires energy and momentum conservation, and in addition, the invariant masses of the two D_s mesons are constrained to the nominal D_s mass, the invariant mass of the $D_s^- \gamma(\pi^0)$ or $D_s^+ \gamma(\pi^0)$ combination is constrained to the nominal D_s^* mass, and the combination

TABLE III. The obtained values of N_{ST}, ϵ_{ST}, and ϵ_{DT} for various signal decays in the ith tag mode, where the efficiencies do not include the branching fractions of the sub-resonant decays and the uncertainties are statistical only. The $\epsilon_{\eta^{(\prime)}} = \epsilon_{\text{DT},\eta^{(\prime)}}/\epsilon_{\text{ST}}$ are the efficiencies of detecting the transition $\gamma(\pi^0)$ and signal channels in the presence of the ST D_s^- candidates.

Tag mode	N_{ST} ($\times 10^3$)	ϵ_{ST} (%)	$\epsilon_{\text{DT},\eta_{\gamma\gamma}}$ (%)	$\epsilon_{\eta_{\gamma\gamma}}$ (%)	$\epsilon_{\text{DT},\eta_{\pi^0\pi^+\pi^-}}$ (%)	$\epsilon_{\eta_{\pi^0\pi^+\pi^-}}$ (%)	$\epsilon_{\text{DT},\eta'_{\eta\pi^+\pi^-}}$ (%)	$\epsilon_{\eta'_{\eta\pi^+\pi^-}}$ (%)	$\epsilon_{\text{DT},\eta'_{\gamma\rho^0}}$ (%)	$\epsilon_{\eta'_{\gamma\rho^0}}$ (%)
$K^+K^-\pi^-$	280.7 ± 0.9	40.87 ± 0.03	18.47 ± 0.05	45.19 ± 0.12	7.11 ± 0.04	17.39 ± 0.10	7.94 ± 0.03	19.43 ± 0.08	9.45 ± 0.05	23.13 ± 0.11
$K^-\pi^+\pi^-$	35.2 ± 1.0	45.38 ± 0.26	20.10 ± 0.08	44.29 ± 0.31	7.78 ± 0.07	17.15 ± 0.18	8.58 ± 0.06	18.91 ± 0.17	10.14 ± 0.08	22.34 ± 0.21
$\pi^-\pi^+\pi^-$	72.7 ± 1.4	51.87 ± 0.16	22.63 ± 0.08	43.63 ± 0.21	8.84 ± 0.08	17.04 ± 0.15	9.84 ± 0.06	18.97 ± 0.13	11.56 ± 0.08	22.29 ± 0.17
$K^+K^-\pi^-\pi^0$	86.3 ± 1.3	11.83 ± 0.03	6.16 ± 0.03	52.03 ± 0.29	2.05 ± 0.02	17.34 ± 0.20	2.43 ± 0.02	20.56 ± 0.18	3.09 ± 0.03	26.09 ± 0.24
$\eta'_{\gamma\rho^0}\pi^-$	50.4 ± 1.0	32.66 ± 0.13	14.51 ± 0.07	44.42 ± 0.27	5.40 ± 0.06	16.54 ± 0.19	6.36 ± 0.05	19.47 ± 0.17	7.43 ± 0.07	22.74 ± 0.22
$\eta_{\gamma\gamma}\rho^-$	80.1 ± 1.9	19.92 ± 0.08	10.04 ± 0.04	50.40 ± 0.28	3.31 ± 0.03	16.62 ± 0.16	4.17 ± 0.03	20.95 ± 0.15	5.31 ± 0.04	26.66 ± 0.21
$K_S^0 K^-\pi^+\pi^-$	15.3 ± 0.4	18.23 ± 0.10	7.85 ± 0.05	43.05 ± 0.37	2.67 ± 0.04	14.63 ± 0.25	2.83 ± 0.03	15.52 ± 0.20	3.57 ± 0.05	19.58 ± 0.28
$K_S^0 K^+\pi^-\pi^-$	29.6 ± 0.3	20.97 ± 0.05	9.15 ± 0.06	43.63 ± 0.29	3.17 ± 0.05	15.12 ± 0.23	3.43 ± 0.04	16.35 ± 0.18	4.52 ± 0.05	21.53 ± 0.26
$\eta_{\gamma\gamma}\pi^-$	39.6 ± 0.8	48.29 ± 0.15	21.73 ± 0.08	44.99 ± 0.22	8.05 ± 0.07	16.67 ± 0.16	9.71 ± 0.06	20.10 ± 0.14	12.10 ± 0.08	25.06 ± 0.19
$K_S^0 K_S^0\pi^-$	10.4 ± 0.2	22.51 ± 0.10	9.57 ± 0.06	42.51 ± 0.32	3.39 ± 0.05	15.07 ± 0.22	3.78 ± 0.04	16.80 ± 0.19	4.78 ± 0.05	21.26 ± 0.26
$\eta_{\pi^0\pi^+\pi^-}\pi^+$	11.7 ± 0.3	23.32 ± 0.11	10.38 ± 0.06	44.53 ± 0.34	3.79 ± 0.05	16.27 ± 0.23	4.36 ± 0.04	18.68 ± 0.20	5.60 ± 0.06	24.03 ± 0.27
$\eta'_{\eta_{\gamma\gamma}\pi^+\pi^-}\pi^-$	19.7 ± 0.2	25.17 ± 0.06	10.94 ± 0.06	43.48 ± 0.27	3.83 ± 0.05	15.22 ± 0.20	4.33 ± 0.04	17.20 ± 0.17	5.64 ± 0.06	22.39 ± 0.24
$K_S^0 K^-\pi^0$	23.0 ± 0.6	16.98 ± 0.09	8.15 ± 0.05	47.99 ± 0.41	2.75 ± 0.04	16.18 ± 0.27	3.48 ± 0.04	20.52 ± 0.25	4.25 ± 0.05	25.04 ± 0.33
$K_S^0 K^-$	62.2 ± 0.4	47.36 ± 0.06	20.46 ± 0.08	43.19 ± 0.18	7.95 ± 0.07	16.78 ± 0.15	9.07 ± 0.06	19.15 ± 0.13	10.69 ± 0.08	22.56 ± 0.17
Average				45.93 ± 0.07		16.86 ± 0.05		19.39 ± 0.04		23.59 ± 0.06

with the smaller χ^2 is kept. To suppress the background contributions from non-$D_s D_s^*$ events in $D_s^+ \to \eta'_{\gamma\rho^0}e^+\nu_e$, the χ^2 is required to satisfy $\chi^2 < 200$.

In the signal side, the η meson is reconstructed by $\eta \to \gamma\gamma$ or $\pi^0\pi^+\pi^-$, and the η' meson is reconstructed by $\eta' \to \eta_{\gamma\gamma}\pi^+\pi^-$ or $\gamma\rho^0_{\pi^+\pi^-}$. The selection criteria of $\eta^{(\prime)}$ are the same as in the ST selection. The positron candidate is identified by using the dE/dx, TOF, and EMC information. Combined likelihoods for the pion, kaon, and positron hypotheses, $\mathcal{L}'_\pi$, $\mathcal{L}'_K$, and $\mathcal{L}'_e$, are calculated. Charged tracks satisfying $\mathcal{L}'_e > 0.001$ and $\mathcal{L}'_e/(\mathcal{L}'_e + \mathcal{L}'_\pi + \mathcal{L}'_K) > 0.8$ are assigned as positron candidates. To suppress background contributions from D_s^+ hadronic decays, the maximum energy of the unused showers ($E_{\gamma\,\text{extra}}^{\max}$) must be less than 0.3 GeV and events with additional charged tracks ($N_{\text{char}}^{\text{extra}}$) are removed. The invariant mass of the $\eta^{(\prime)}$ and e^+ is required to be $M_{\eta^{(\prime)}e^+} < 1.9$ GeV/c^2 for $D_s^+ \to \eta^{(\prime)}e^+\nu_e$ to further suppress the background contributions of $D_s^+ \to \eta^{(\prime)}\pi^+$. To suppress contributions of backgrounds to $D_s^+ \to \eta'_{\gamma\rho^0}e^+\nu_e$ where the photon is from a π^0 decay, the opening angle between the missing momentum and the most energetic unused shower ($\theta_{\gamma,\text{miss}}$) is required to satisfy $\cos\theta_{\gamma,\text{miss}} < 0.85$.

VI. BRANCHING FRACTIONS

A. Results of branching fractions

After imposing all selection criteria, the M_{miss}^2 distributions of the accepted candidates for the semileptonic decays $D_s^+ \to \eta^{(\prime)}e^+\nu_e$ are obtained, as shown in Fig. 2. For the semileptonic D_s^+ decays reconstructed via two different $\eta^{(\prime)}$ decays, a simultaneous unbinned maximum-likelihood fit is performed on the two M_{miss}^2 distributions, where the

branching fractions of $D_s^+ \to \eta^{(\prime)}e^+\nu_e$ measured with the different $\eta^{(\prime)}$ decay modes are constrained to be equal. The signal and background components are modeled with shapes derived from MC simulation. The yields of the peaking backgrounds due to $D_s^+ \to \eta^{(\prime)}\pi^+\pi^0$ and $\eta^{(\prime)}\mu^+\nu_\mu$ are fixed according to the MC simulation. For $D_s^+ \to \eta'_{\gamma\rho^0}e^+\nu_e$, there is a remaining background contribution from $D_s^+ \to \phi(1020)_{\pi^0\pi^+\pi^-}e^+\nu_e$. The yield of $D_s^+ \to \phi(1020)_{\pi^0\pi^+\pi^-}e^+\nu_e$ is left free in the fit. The remaining combinatorial backgrounds are dominated by open charm (more than 60%) and $e^+e^- \to q\bar{q}$ (about 30%). The magnitude of this contribution is a free parameter in the fit. The branching fractions of the intermediate decays are $\mathcal{B}(\eta \to \gamma\gamma) = (39.36 \pm 0.18)\%$, $\mathcal{B}(\eta \to \pi^0\pi^+\pi^-) = (23.02 \pm 0.25)\%$, $\mathcal{B}(\eta' \to \eta\pi^+\pi^-) = (42.5 \pm 0.5)\%$, $\mathcal{B}(\eta' \to \pi^+\pi^-\gamma) = (29.5 \pm 0.4)\%$, and $\mathcal{B}(\pi^0 \to \gamma\gamma) = (98.823 \pm 0.034)\%$ [13]. The branching fractions of $D_s^+ \to \eta^{(\prime)}e^+\nu_e$, the yields of other background contributions and the parameters of the Gaussian functions convolved with the distributions from MC simulation are left free during the fit. The branching fractions are calculated from the signal yields with Eq. (1). The signal efficiencies, the signal yields, and the obtained branching fractions are summarized in Table IV.

B. Systematic uncertainties

Table V summarizes the sources of the systematic uncertainties in the measurements of the branching fractions of $D_s^+ \to \eta^{(\prime)}e^+\nu_e$. They are assigned relative to the measured branching fractions and are discussed below. In this table, the contributions to the systematic uncertainties listed in the upper part are treated as correlated, while those in the lower part are treated as uncorrelated.
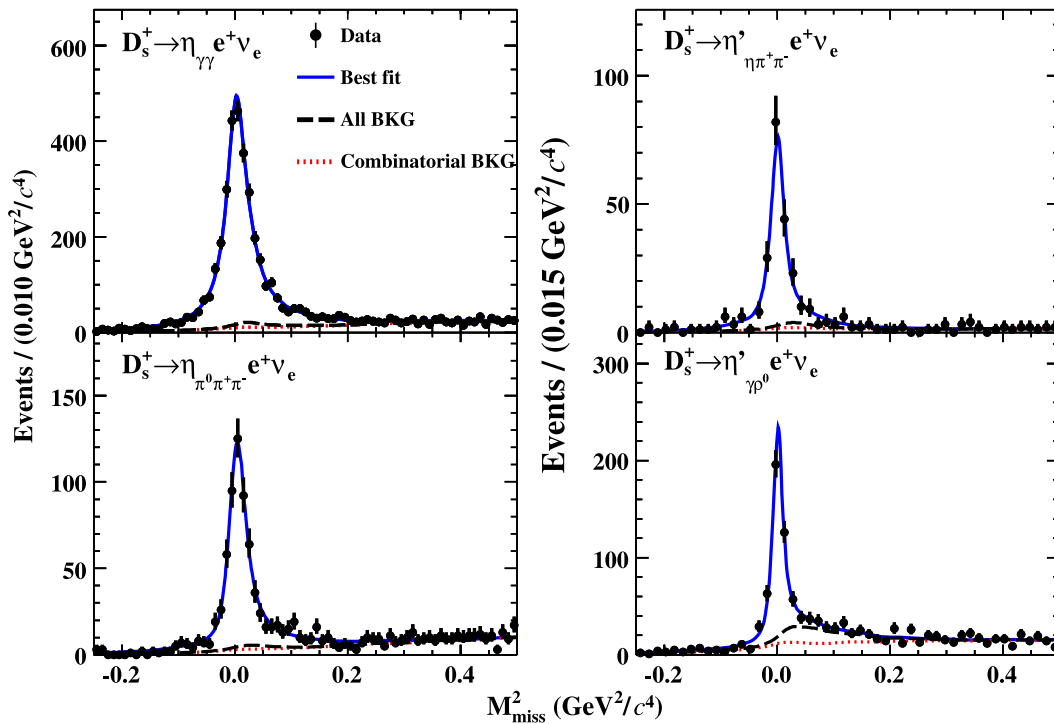
FIG. 2. Fits to the M_{miss}^2 distributions of the candidate events for various semileptonic decays. The points with error bars represent data. The blue solid curves denote the total fits, and the red solid dotted curves show the fitted combinatorial background contributions. Differences between dashed and dotted curves are the backgrounds from $D_s^+ \to \eta^{(\prime)} \pi^+ \pi^0$, $\eta^{(\prime)} \mu^+ \nu_\mu$, and $D_s^+ \to \phi(1020)_{\pi^0 \pi^+ \pi^-} e^+ \nu_e$.

The total systematic uncertainties of the branching fractions of $D_s^+ \to \eta e^+ \nu_e$ and $D_s^+ \to \eta' e^+ \nu_e$ are calculated to be 2.3% and 2.9%, respectively, after taking into account correlated and uncorrelated systematic uncertainties and using the method described in Ref. [44].

(a) *ST D_s^- yields*: The uncertainty of the fits to the D_s^- invariant mass spectra is estimated by varying the signal and background shapes and repeating the fits for both data and MC sample. A variation of the signal shape is obtained by modifying the matching requirement between generated and reconstructed angles from 15° to 10° or 20°. The background shape is changed to a third-order Chebychev polynomial. The

relative change of the ST yields in data over the ST efficiencies is considered as the systematic uncertainty. Moreover, an additional uncertainty due to the background fluctuation of the fitted ST yields is included. The quadrature sum of these three terms, 0.5%, is assigned as the associated systematic uncertainty.

(b) π^0 *and η reconstruction*: The systematic uncertainty in the π^0 reconstruction has been studied by using the control sample of $e^+ e^- \to K^+ K^- \pi^+ \pi^- \pi^0$. The systematic uncertainty in the η reconstruction is taken as equal to that of the π^0 due to the limited η sample. After correcting differences of the π^0 or η reconstruction efficiencies between data and MC simulation, which are 0.991–1.024, the systematic uncertainties, due to statistical uncertainties on these corrections, are listed in Table V.

(c) $\pi^\pm$ *tracking and PID efficiencies*: The tracking and PID efficiencies of $\pi^\pm$ are studied by using the control sample of $e^+ e^- \to K^+ K^- \pi^+ \pi^-$. The momentum weighted data-MC differences due to $\pi^\pm$ tracking efficiencies range from 0.981–1.001 for different signal decays and the signal efficiencies are corrected by these factors. The systematic uncertainties due to $\pi^\pm$ tracking and $\pi^\pm$ PID are listed in Table V. The uncertainties of $\pi^\pm$ tracking for $D_s^+ \to \eta'_{\eta\pi^+\pi^-} e^+ \nu_e$ and $D_s^+ \to \eta'_{\gamma\rho^0} e^+ \nu_e$ are partly correlated, the common

TABLE IV. Signal efficiencies ($\epsilon_{\gamma(\pi^0)SL}$), signal yields ($N_{DT}$), and obtained branching fractions ($\mathcal{B}_{SL}$) for various semielectronic decays. Efficiencies include the branching fractions of $D_s^{*\mp}$ decays but do not include the branching fractions of the $\eta^{(\prime)}$ decays. Numbers in the first and second parentheses are the statistical and systematic uncertainties, respectively.

Decay	$\eta^{(\prime)}$ decays	$\epsilon_{\gamma(\pi^0)SL}$ (%)	N_{DT}	$\mathcal{B}_{SL}$ (%)
$\eta e^+ \nu_e$	$\gamma\gamma$	45.93(07)	4036(71)	2.255(39)(51)
	$\pi^0 \pi^+ \pi^-$	16.86(05)		
$\eta' e^+ \nu_e$	$\eta\pi^+\pi^-$	19.39(04)	675(32)	0.810(38)(24)
	$\gamma\rho^0$	23.59(06)		

TABLE V. Relative systematic uncertainties (in %) on the measurements of the branching fractions of $D_s^+ \to \eta e^+ \nu_e$ and $D_s^+ \to \eta' e^+ \nu_e$. The top and the bottom sections are correlated and uncorrelated, respectively. The uncertainty in the uncorrelated $\pi^\pm$ tracking is obtained as the square root of the quadratic difference of the total uncertainty in the $\pi^\pm$ tracking and the correlated portion.

Source	$\eta_{\gamma\gamma} e^+ \nu_e$	$\eta_{\pi^0\pi^+\pi^-} e^+ \nu_e$	$\eta'_{\eta\pi^+\pi^-} e^+ \nu_e$	$\eta'_{\gamma\rho^0} e^+ \nu_e$
ST D_s^- yields	0.5	0.5	0.5	0.5
π^0 and η reconstruction	1.1	1.1	0.8	$\cdots$
$\pi^\pm$ tracking	$\cdots$	1.2	0.6	0.6
$\pi^\pm$ PID	$\cdots$	0.4	0.4	0.4
$e^\pm$ tracking	0.5	0.5	0.5	0.5
$e^\pm$ PID	0.2	0.2	0.2	0.2
Transition $\gamma(\pi^0)$ reconstruction	1.0	1.0	1.0	1.0
Smallest $|\Delta E|$	1.0	1.0	1.0	1.0
Peaking background	0.4	0.4	1.0	1.0
Hadronic transition form factors	0.5	0.5	0.2	0.2
$\pi^\pm$ tracking	$\cdots$	$\cdots$	1.7	$\cdots$
$\eta^{(\prime)}$ selection	$\cdots$	0.1	0.1	1.4
Tag bias	0.4	0.1	0.1	0.1
χ^2 requirement	$\cdots$	$\cdots$	$\cdots$	1.5
$M_{\eta^{(\prime)}e^+}$ requirement	Neglected	Neglected	Neglected	Neglected
$\cos\theta_{\gamma,\text{miss}}$ requirement	Neglected	Neglected	Neglected	Neglected
$E_{\text{extra}\gamma}^{\max}$ and $N_{\text{extra}}^{\text{char}}$ requirements	0.7	2.0	2.0	1.1
M_{miss}^2 fit	0.4	0.7	0.7	0.5
MC statistics	0.1	0.3	0.2	0.2
Quoted branching fractions	0.5	1.1	1.3	1.4
Total	2.3	3.4	3.7	3.4

uncertainty of 0.6% is considered as fully correlated, and the remaining quadratic difference of 1.7% for $D_s^+ \to \eta'_{\eta\pi^+\pi^-} e^+ \nu_e$ is uncorrelated.

(d) *$e^\pm$ tracking and PID efficiencies*: The e^+ tracking and PID efficiencies are studied by using the control sample of $e^+ e^- \to \gamma e^+ e^-$. The ratios are 1.000 ± 0.005 for $e^\pm$ tracking and 0.988 ± 0.002 for $e^\pm$ PID efficiencies. After corrections, the systematic uncertainties, due to statistical uncertainties on these factors, are listed in Table V.

(e) *Transition $\gamma(\pi^0)$ reconstruction*: The systematic uncertainty of the transition $\gamma(\pi^0)$ selection is assigned as 1.0% based on studies of the control sample of $J/\psi \to \pi^0 \pi^+ \pi^-$ [45].

(f) *Smallest $|\Delta E|$*: The systematic uncertainty of selecting the transition $\gamma(\pi^0)$ with the smallest $|\Delta E|$ method is studied by using two control samples of $D_s^+ \to K^+ K^- \pi^+$ and $D_s^+ \to \eta \pi^0 \pi^+$. The difference of the efficiency of selecting the transition $\gamma(\pi^0)$ candidates in data versus the simulation is 1.0%, which is assigned as the systematic uncertainty.

(g) *Peaking background*: The systematic uncertainty due to the peaking backgrounds from $D_s^+ \to \eta^{(\prime)} \pi^+ \pi^0$ and $D_s^+ \to \eta^{(\prime)} \mu^+ \nu_\mu$ is estimated by varying the quoted branching fractions [13] by $\pm 1\sigma$ and correcting by the data-MC difference for the misidentification of

$\pi^+ \to e^+$ and $\mu^+ \to e^+$. The relative changes of signal yields are taken as the corresponding systematic uncertainties and listed in Table V.

(h) *Hadronic transition form factors*: The detection efficiencies are estimated by using signal MC events generated with the hadronic transition form factors measured in this work. The corresponding systematic uncertainties are estimated by varying the parameters by $\pm 1\sigma$ and listed in Table V.

(i) *$\eta^{(\prime)}$ selection*: The systematic uncertainties due to the $\eta^{(\prime)}$ invariant mass requirements are estimated to be 0.1%, 0.1%, and 1.0% for $D_s^+ \to \eta_{\pi^0\pi^+\pi^-} e^+ \nu_e$, $D_s^+ \to \eta'_{\eta\pi^+\pi^-} e^+ \nu_e$, and $D_s^+ \to \eta'_{\gamma\rho^0} e^+ \nu_e$, respectively, by analyzing the difference of the resolution of $M_{\eta^{(\prime)}}$ between data and MC simulation with the sample $J/\psi \to \phi \eta^{(\prime)}$. Additionally, a 1.0% uncertainty, related to the γ reconstruction efficiency in the $\eta' \to \gamma \rho^0$ decay, is estimated by studying a control sample of $J/\psi \to \pi^0 \pi^+ \pi^-$ [45].

(j) *Tag bias*: Due to different reconstruction environments in the inclusive and signal MC samples, the ST efficiencies determined by the inclusive MC sample may be different from those by the signal MC sample. This may lead to incomplete cancellation of the systematic uncertainties associated with the ST selection, referred to as "tag bias." Inclusive and signal MC

efficiencies are compared and the tracking and PID efficiencies for kaons and pions are studied for different track multiplicities. The resulting ST-average offsets are assigned as the systematic uncertainties from tag bias and listed in Table V.

(k) χ^2 *requirement*: The systematic uncertainty due to the χ^2 requirement is estimated with a hadronic DT sample with $D_s^+ \to \eta'_{\gamma\rho^0}\pi^+$ replacing the semileptonic signal. The difference of the accepted efficiencies of the χ^2 requirement between data and MC simulation is 1.5%, which is assigned as the systematic uncertainty for $D_s^+ \to \eta'_{\gamma\rho^0}e^+\nu_e$.

(l) $M_{\eta^{(\prime)}e^+}$ *requirement*: The efficiencies of the $M_{\eta^{(\prime)}e^+} < 1.9 \text{ GeV}/c^2$ requirement are greater than 99% for all signal decays and the differences of these efficiencies between data and MC simulation are negligible.

(m) $\cos\theta_{\gamma,\text{miss}}$ *requirement*: The systematic uncertainty due to the $\cos\theta_{\gamma,\text{miss}}$ requirement is estimated by varying the requirement by ± 0.05. The differences of the branching fractions are negligible.

(n) $E_{\text{extra}\gamma}^{\max}$ *and* $N_{\text{extra}}^{\text{char}}$ *requirements*: The systematic uncertainty in the $E_{\text{extra}\gamma}^{\max}$ and $N_{\text{extra}}^{\text{char}}$ requirements is estimated with a hadronic DT sample with $D_s^+ \to \eta_{\gamma\gamma}\pi^+$, $\eta_{\pi^0\pi^+\pi^-}\pi^+$, $\eta'_{\eta\pi^+\pi^-}\pi^+$, and $\eta'_{\gamma\rho^0}\pi^+$. The associated systematic uncertainties are listed in Table V.

(o) M_{miss}^2 *fit*: The systematic uncertainty due to the M_{miss}^2 fit is considered in two parts. Since a Gaussian function is convolved with the simulated signal shapes to account for the resolution difference between data and MC simulation, the systematic uncertainty from the signal shape is ignored. The systematic uncertainty due to the background shape is assigned by varying the relative fractions of major backgrounds from $e^+e^- \to q\bar{q}$ and non-$D_s^{*\pm}D_s^{\mp}$ open-charm processes within $\pm 30\%$ according to the uncertainty of its input cross section in the inclusive MC sample. The changes in the branching fractions are taken as the corresponding systematic uncertainties and listed in Table V.

(p) *MC statistics*: The relative uncertainties of the signal efficiencies are assigned as the systematic uncertainties due to MC statistics, as listed in Table V.

(q) *Quoted branching fractions*: The uncertainties in the quoted branching fractions of $\pi^0 \to \gamma\gamma$, $\eta \to \gamma\gamma$, $\eta \to \pi^0\pi^+\pi^-$, $\eta' \to \eta\pi^+\pi^-$, and $\eta' \to \pi^+\pi^-\gamma$ are 0.03%, 0.5%, 1.1%, 1.2%, and 1.4%, respectively. The quoted branching fraction of $D_s^{*+} \to \pi^0 D_s^+$ is measured relative to $D_s^{*+} \to \gamma D_s^+$. Thus, they are fully correlated with each other and their uncertainty is 0.7%. The change in signal detection efficiency when changing these branching fractions by $\pm 1\sigma$ is at most 0.1%, which is assigned as the systematic uncertainty. Quadratically summing these two effects gives the associated systematic uncertainties 0.5%, 1.1%, 1.3%,

and 1.4% for $D_s^+ \to \eta_{\gamma\gamma}e^+\nu_e$, $D_s^+ \to \eta_{\pi^0\pi^+\pi^-}e^+\nu_e$, $D_s^+ \to \eta'_{\eta\pi^+\pi^-}e^+\nu_e$, and $D_s^+ \to \eta'_{\gamma\rho^0}e^+\nu_e$, respectively.

VII. HADRONIC TRANSITION FORM FACTORS

The differential decay width can be expressed as

$$\frac{d\Gamma(D_s^+ \to \eta^{(\prime)}e^+\nu_e)}{dq^2} = \frac{G_F^2|V_{cs}|^2}{24\pi^3}\left|f_+^{\eta^{(\prime)}}(q^2)\right|^2 |\vec{p}_{\eta^{(\prime)}}|^3, \quad (4)$$

where q is the momentum transfer to the $e^+\nu_e$ system, $|\vec{p}_{\eta^{(\prime)}}|$ is the magnitude of the meson 3-momentum in the D_s^+ rest frame and G_F is the Fermi constant. In the modified pole model [46],

$$f_+^{\eta^{(\prime)}}(q^2) = \frac{f_+^{\eta^{(\prime)}}(0)}{\left(1 - \frac{q^2}{M_{\text{pole}}^2}\right)\left(1 - \alpha\frac{q^2}{M_{\text{pole}}^2}\right)}, \quad (5)$$

where M_{pole} is fixed to $m_{D_s^{*+}}$ and α is a free parameter. The simple pole model [47] is obtained by setting $\alpha = 0$ and leaving M_{pole} free. In the two-parameter (2-Par) series expansion [46], the hadronic transition form factor is given by

$$f_+^{\eta^{(\prime)}}(q^2) = \frac{1}{P(q^2)\Phi(q^2)}\frac{f_+^{\eta^{(\prime)}}(0)P(0)\Phi(0)}{1 + r_1(t_0)z(0,t_0)} \times \left(1 + r_1(t_0)[z(q^2,t_0)]\right). \quad (6)$$

Here, $P(q^2) = z(q^2, m_{D_s^*}^2)$, where $z(q^2,t_0) = \frac{\sqrt{t_+ - q^2} - \sqrt{t_+ - t_0}}{\sqrt{t_+ - q^2} + \sqrt{t_+ - t_0}}$. Φ is given by

$$\Phi(q^2) = \sqrt{\frac{1}{24\pi\chi_V}}\left(\frac{t_+ - q^2}{t_+ - t_0}\right)^{1/4}\left(\sqrt{t_+ - q^2} + \sqrt{t_+}\right)^{-5}$$
$$\times \left(\sqrt{t_+ - q^2} + \sqrt{t_+ - t_0}\right)$$
$$\times \left(\sqrt{t_+ - q^2} + \sqrt{t_+ - t_-}\right)^{3/2}(t_+ - q^2)^{3/4}, \quad (7)$$

where $t_\pm = (m_{D_s^+} \pm m_{\eta^{(\prime)}})^2$, $t_0 = t_+(1 - \sqrt{1 - t_-/t_+})$, $m_{D_s^+}$ and $m_{\eta^{(\prime)}}$ are the masses of D_s^+ and $\eta^{(\prime)}$ particles, $m_{D_s^*}$ is the pole mass of the vector form factor accounting for the strong interaction between D_s^+ and $\eta^{(\prime)}$ mesons and usually taken as the mass of the lowest lying $c\bar{s}$ vector meson D_s^* [13], and χ_V is obtained from dispersion relations using perturbative QCD [48].

A. Differential decay rates

To extract the hadronic transition form factors of the semileptonic decays, the differential decay rates are measured in different q^2 intervals. For the $D_s^+ \to \eta e^+\nu_e$ decay,

TABLE VI.   Summary of efficiency correction factors, f_{corr}^i, in each q^2 bin.

q^2	$D_s^+ \to \eta_{\gamma\gamma} e^+ \nu_e$	$D_s^+ \to \eta_{\pi^0 \pi^+ \pi^-} e^+ \nu_e$	$D_s^+ \to \eta'_{\eta \pi^+ \pi^-} e^+ \nu_e$	$D_s^+ \to \eta'_{\gamma\rho^0} e^+ \nu_e$
1	0.980 ± 0.018	0.996 ± 0.012	0.967 ± 0.014	0.981 ± 0.005
2	0.978 ± 0.016	0.997 ± 0.012	0.971 ± 0.015	0.980 ± 0.005
3	0.976 ± 0.013	0.996 ± 0.013	0.976 ± 0.017	0.979 ± 0.005
4	0.973 ± 0.011	0.997 ± 0.014	$\cdots$	$\cdots$
5	0.971 ± 0.010	0.998 ± 0.016	$\cdots$	$\cdots$
6	0.974 ± 0.009	0.998 ± 0.017	$\cdots$	$\cdots$
7	0.978 ± 0.009	0.998 ± 0.019	$\cdots$	$\cdots$
8	0.990 ± 0.009	0.996 ± 0.023	$\cdots$	$\cdots$

the q^2 range $(m_e^2, 2.02)$ GeV$^2/c^4$ is subdivided in eight intervals of 0.2 GeV$^2/c^4$ width (except for a wider final bin), while three regions, $(m_e^2, 0.3)$, $(0.3, 0.6)$, and $(0.6, 1.02)$ GeV$^2/c^4$, are defined for $D_s^+ \to \eta' e^+ \nu_e$. The differential decay rates in the individual q^2 intervals i are determined as

$$\frac{d\Gamma_i}{dq_i^2} = \frac{\Delta\Gamma_i}{\Delta q_i^2}, \qquad (8)$$

where $\Delta\Gamma_i = \frac{N_{\mathrm{prd}}^i}{\tau_{D_s^+} \cdot N_{\mathrm{ST}}}$ is the decay rate in the ith q^2 interval, N_{prd}^i is the number of events produced in the ith q^2 interval, $\tau_{D_s^+}$ is the D_s^+ lifetime [13] and N_{ST} is the number of the ST D_s^- mesons.

In the ith q^2 interval, the number of events produced in data is calculated as

$$N_{\mathrm{prd}}^i = \sum_{j}^{N_{\mathrm{intervals}}} (\varepsilon^{-1})_{ij} N_{\mathrm{DT}}^j, \qquad (9)$$

where $(\varepsilon^{-1})_{ij}$ is the element of the inverse efficiency matrix, obtained by analyzing the signal MC events. The statistical uncertainty of N_{prd}^i is given by

$$[\sigma(N_{\mathrm{prd}}^i)]^2 = \sum_{j}^{N_{\mathrm{intervals}}} (\varepsilon^{-1})_{ij}^2 [\sigma_{\mathrm{stat}}(N_{\mathrm{DT}}^j)]^2, \qquad (10)$$

where $\sigma_{\mathrm{stat}}(N_{\mathrm{DT}}^j)$ is the statistical uncertainty of N_{DT}^j. The efficiency matrix ε_{ij} is given by

$$\varepsilon_{ij} = \frac{N_{ij}^{\mathrm{rec}}}{N_j^{\mathrm{gen}}} \cdot \frac{1}{\varepsilon_{\mathrm{tag}}} \cdot f_j^{\mathrm{corr}}, \qquad (11)$$

where N_{ij}^{rec} is the number of events generated in the jth q^2 interval and reconstructed in the ith q^2 interval, N_j^{gen} is the total number of events generated in the jth q^2 interval, and $\varepsilon_{\mathrm{tag}}$ is the ST efficiency. f_j^{corr} is the efficiency correction factor for the events generated in the jth q^2 interval, which is obtained with the same analysis procedure as that in the branching fraction measurement. The product of the efficiency correction factors in each q^2 is listed in Table VI.

Tables VII and VIII give the elements of the efficiency matrices weighted by the ST yields in the data sample.

The number of events observed in each reconstructed q^2 interval is obtained from a fit to the M_{miss}^2 distribution of the corresponding events. Figures 3 and 4 show the results of the fits to the M_{miss}^2 distributions in the reconstructed q^2 intervals. Tables IX and X summarize the q^2 ranges, the

TABLE VII.   The efficiency matrices for $D_s^+ \to \eta e^+ \nu_e$ averaged over all 14 ST modes, where ε_{ij} represents the efficiency in % for events produced in the jth q^2 interval and reconstructed in the ith q^2 interval. Efficiencies do not include the branching fractions of $\eta^{(\prime)}$.

	$D_s^+ \to \eta_{\gamma\gamma} e^+ \nu_e$								$D_s^+ \to \eta_{\pi^0 \pi^+ \pi^-} e^+ \nu_e$							
ε_{ij}	1	2	3	4	5	6	7	8	1	2	3	4	5	6	7	8
1	43.65	4.46	0.41	0.06	0.01	0.00	0.00	0.00	17.50	1.63	0.16	0.02	0.00	0.00	0.00	0.00
2	3.33	38.17	5.09	0.60	0.10	0.02	0.01	0.01	1.22	15.10	1.71	0.24	0.03	0.00	0.00	0.00
3	0.26	3.97	36.08	5.17	0.61	0.11	0.02	0.01	0.12	1.47	14.04	1.56	0.23	0.02	0.00	0.00
4	0.07	0.32	4.40	35.14	5.09	0.54	0.09	0.02	0.04	0.19	1.55	13.01	1.48	0.21	0.02	0.00
5	0.04	0.09	0.35	4.36	34.36	4.96	0.46	0.05	0.02	0.07	0.17	1.61	12.40	1.38	0.17	0.01
6	0.02	0.05	0.11	0.35	4.25	34.21	4.82	0.28	0.01	0.03	0.05	0.19	1.53	11.89	1.27	0.06
7	0.02	0.03	0.05	0.11	0.33	3.94	34.54	2.69	0.01	0.01	0.02	0.07	0.17	1.45	11.12	0.65
8	0.02	0.04	0.03	0.08	0.17	0.40	3.68	40.71	0.00	0.01	0.02	0.03	0.08	0.27	1.50	11.99

TABLE VIII. The efficiency matrices for $D_s^+ \to \eta' e^+ \nu_e$ averaged over all 14 ST modes, where ε_{ij} represents the efficiency in % for events produced in the jth q^2 interval and reconstructed in the ith q^2 interval. Efficiencies do not include the branching fractions of $\eta^{(\prime)}$ subdecays.

ε_{ij}	$D_s^+ \to \eta'_{\eta\pi^+\pi^-} e^+\nu_e$			$D_s^+ \to \eta'_{\gamma\rho^0} e^+\nu_e$		
	1	2	3	1	2	3
1	18.74	1.53	0.06	22.39	1.65	0.08
2	0.77	16.99	1.70	0.75	21.54	1.78
3	0.01	0.67	17.47	0.05	0.75	22.20

fitted numbers of observed DT events (N_{DT}), the numbers of generated events (N_{prd}) calculated by the weighted efficiency matrix and the decay rates of $D_s^+ \to \eta^{(\prime)} e^+ \nu_e$ ($\Delta\Gamma$) in the individual q^2 intervals.

B. χ^2 construction and statistical covariance matrices

To extract the hadronic transition form factor parameters and $|V_{cs}|$, the smallest χ^2 method is used to fit the partial decay rates of the different signal decays. Considering the correlations of the measured partial decay rates ($\Delta\Gamma_i^{\mathrm{msr}}$) among different q^2 intervals, the χ^2 is given by

$$\chi^2 = \sum_{i,j=1}^{N_{\mathrm{intervals}}} \left(\Delta\Gamma_i^{\mathrm{msr}} - \Delta\Gamma_i^{\mathrm{th}}\right) C_{ij}^{-1} \left(\Delta\Gamma_j^{\mathrm{msr}} - \Delta\Gamma_j^{\mathrm{th}}\right), \quad (12)$$

where $\Delta\Gamma_i^{\mathrm{th}}$ is the theoretically expected decay rate in channel i, C_{ij} is the element of the covariance matrix of the measured partial decay rates and it is given by $C_{ij} = C_{ij}^{\mathrm{stat}} + C_{ij}^{\mathrm{sys}}$. Here, C_{ij}^{stat} and C_{ij}^{sys} are elements of the statistical and systematic covariance matrices, respectively. The elements of the statistical covariance matrix are defined as

$$C_{ij}^{\mathrm{stat}} = \left(\frac{1}{\tau_{D_s^+} N_{\mathrm{tag}}}\right)^2 \sum_\alpha \varepsilon_{i\alpha}^{-1} \varepsilon_{j\alpha}^{-1} \left(\sigma(N_{\mathrm{DT}}^\alpha)\right)^2. \quad (13)$$

Tables XIII and XIV give the elements of the statistical correction density matrices for $D_s^+ \to \eta_{\gamma\gamma} e^+ \nu_e$, $D_s^+ \to \eta_{\pi^0\pi^+\pi^-} e^+ \nu_e$, $D_s^+ \to \eta'_{\eta\pi^+\pi^-} e^+ \nu_e$, and $D_s^+ \to \eta'_{\gamma\rho^0} e^+ \nu_e$, respectively.

C. Systematic uncertainties

Several sources of systematic uncertainties are discussed below.

(a) D_s^+ *lifetime*: The uncertainties associated with the D_s^+ lifetime are fully correlated across the q^2 intervals. The
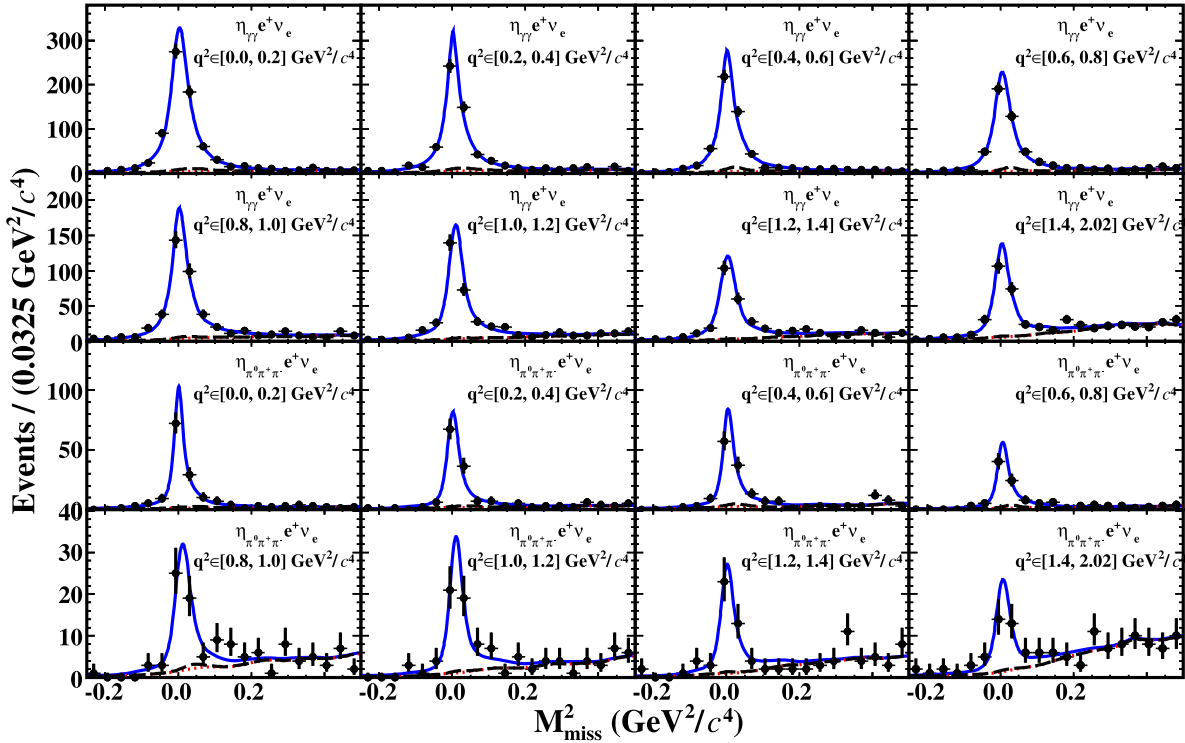

FIG. 3. Fits to the M_{miss}^2 distributions in various reconstructed q^2 intervals for (top two rows) $D_s^+ \to \eta_{\gamma\gamma} e^+ \nu_e$ and (bottom two rows) $D_s^+ \to \eta_{\pi^0\pi^+\pi^-} e^+ \nu_e$. The points with error bars represent data. The blue solid curves denote the total fits, and the red solid dotted curves show the fitted combinatorial background contributions. Differences between black dashed and red dotted curves show the backgrounds from $D_s^+ \to \eta\pi^+\pi^0$ and $\eta\mu^+\nu_\mu$.

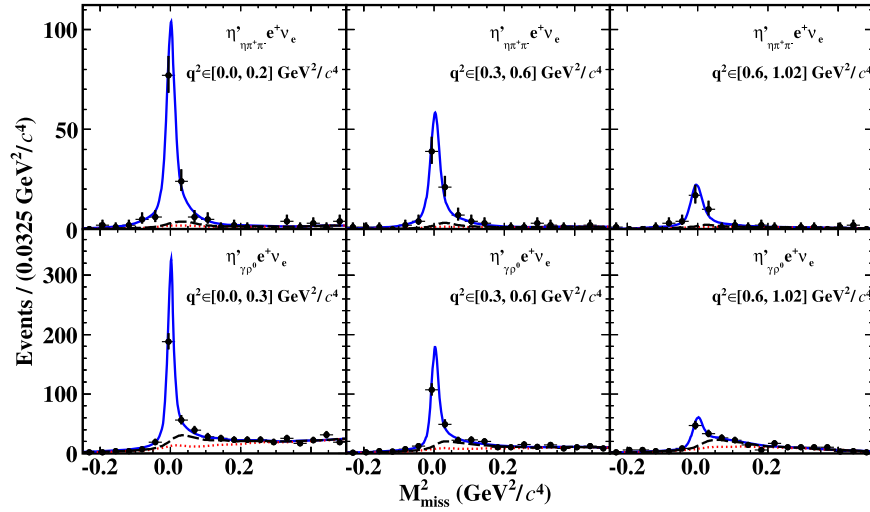FIG. 4. Fits to the M_{miss}^2 distributions in various reconstructed q^2 intervals for (top row) $D_s^+ \to \eta'_{\eta\pi^+\pi^-} e^+\nu_e$ and (bottom row) $D_s^+ \to \eta'_{\gamma\rho^0} e^+\nu_e$. The points with error bars represent data. The blue solid curves denote the total fits and the red solid dotted curves show the fitted combinatorial background contributions. Differences between black dashed and red dotted curves are the backgrounds from $D_s^+ \to \eta'\pi^+\pi^0$, $\eta'\mu^+\nu_\mu$, and $D_s^+ \to \phi(1020)_{\pi^0\pi^+\pi^-} e^+\nu_e$.

element of the related systematic covariance matrix is calculated by

$$C_{ij}^{\text{sys}}(\tau_{D_s^+}) = \sigma(\Delta\Gamma_i)\sigma(\Delta\Gamma_j), \quad (14)$$

where $\sigma(\Delta\Gamma_i) = \sigma\tau_{D_s^+} \cdot \Delta\Gamma_i$ and $\sigma\tau_{D_s^+}$ is the uncertainty of the D_s^+ lifetime [13].

(b) *MC statistics*: Systematic efficiency uncertainties in and correlations between the q^2 intervals due to the limited MC size are calculated by

$$C_{ij}^{\text{sys}} = \left(\frac{1}{\tau_{D_s^+} N_{\text{tag}}}\right)^2 \sum_{\alpha\beta} N_{\text{DT}}^\alpha N_{\text{DT}}^\beta \text{Cov}\left(\varepsilon_{i\alpha}^{-1}, \varepsilon_{j\beta}^{-1}\right), \quad (15)$$

where the covariances of the inverse efficiency matrix elements are given by [49]

$$\text{Cov}\left(\varepsilon_{i\alpha}^{-1}, \varepsilon_{j\beta}^{-1}\right) = \sum_{mn} \left(\varepsilon_{im}^{-1}\varepsilon_{jm}^{-1}\right)[\sigma(\epsilon_{mn})]^2\left(\varepsilon_{\alpha n}^{-1}\varepsilon_{\beta n}^{-1}\right). \quad (16)$$

TABLE IX. The partial decay rates of $D_s^+ \to \eta e^+\nu_e$ in various q^2 intervals. Numbers in the parentheses are the statistical uncertainties.

i q^2 (GeV^2/c^4)		1 $(m_e^2, 0.2)$	2 (0.2, 0.4)	3 (0.4, 0.6)	4 (0.6, 0.8)	5 (0.8, 1.0)	6 (1.0, 1.2)	7 (1.2, 1.4)	8 (1.4, 2.02)
$D_s^+ \to \eta_{\gamma\gamma} e^+\nu_e$	N_{obs}^i	681(28)	550(26)	497(25)	455(24)	371(21)	316(20)	252(18)	260(19)
	N_{prd}^i	3637(167)	2929(179)	2740(181)	2578(180)	2092(167)	1826(154)	1497(137)	1446(118)
	$\Delta\Gamma_{\text{msr}}^i$ (ns^{-1})	8.83(40)	7.11(43)	6.66(44)	6.26(44)	5.08(41)	4.43(37)	3.64(33)	3.51(29)
$D_s^+ \to \eta_{\pi^0\pi^+\pi^-} e^+\nu_e$	N_{DT}^i	132(12)	123(12)	120(12)	83(10)	58(09)	57(09)	47(08)	42(08)
	N_{prd}^i	3019(316)	2951(365)	3153(400)	2169(359)	1486(345)	1688(337)	1500(317)	1298(303)
	$\Delta\Gamma_{\text{msr}}^i$ (ns^{-1})	7.33(77)	7.17(89)	7.66(97)	5.27(87)	3.61(84)	4.10(82)	3.64(77)	3.15(73)

TABLE X. The partial decay rates of $D_s^+ \to \eta' e^+\nu_e$ in various q^2 intervals. Numbers in the parentheses are the statistical uncertainties.

i q^2 (GeV^2/c^4)		1 $(m_e^2, 0.3)$	2 (0.3, 0.6)	3 (0.6, 1.02)
$D_s^+ \to \eta'_{\eta_{\gamma\gamma}\pi^+\pi^-} e^+\nu_e$	N_{obs}^i	116(12)	72(09)	32(07)
	N_{prd}^i	3528(371)	2258(331)	991(226)
	$\Delta\Gamma_{\text{msr}}^i$ (ns^{-1})	8.57(90)	5.48(80)	2.41(55)
$D_s^+ \to \eta'_{\gamma\rho^0} e^+\nu_e$	N_{DT}^i	237(19)	157(16)	63(14)
	N_{prd}^i	3411(286)	2281(251)	879(217)
	$\Delta\Gamma_{\text{msr}}^i$ (ns^{-1})	8.28(69)	5.54(61)	2.14(53)

(c) *Hadronic transition form factor*: Systematic uncertainties associated with the hadronic transition form factor used to generate signal MC events are estimated by reweighting the signal MC events so that the q^2 spectrum agrees with the measured spectrum. For each signal MC event, the weight ω is given by

$$\omega = \frac{\left|f_+^{\eta^{(\prime)} \text{measured}}(q^2)\right|^2 \int_{q_{\min}^2}^{q_{\max}^2} \frac{d\Gamma^{\text{default}}}{dq^2} dq^2}{\left|f_+^{\eta^{(\prime)} \text{default}}(q^2)\right|^2 \int_{q_{\min}^2}^{q_{\max}^2} \frac{d\Gamma^{\text{measured}}}{dq^2} dq^2}, \quad (17)$$

where $f_+^{\eta^{(\prime)} \text{default}}(q^2)$ is the default hadronic transition form factor used to generate the signal MC events. The default hadronic transition form factor uses the modified pole model with the parameter $\alpha = 0.25$ and $f_+(0) = 1.0$. The $f_+^{\eta^{(\prime)} \text{measured}}(q^2)$ is the measured hadronic transition form factor for $D_s^+ \to \eta^{(\prime)} e^+ \nu_e$ using the 2-Par series expansion with parameters obtained from the fit with the statistical covariance matrix.

The partial decay rates are then calculated in different q^2 intervals with the newly weighted efficiency matrix. The element of the covariance matrix is defined as

$$C_{ij}^{\text{sys}}(\text{FF}) = \delta(\Delta\Gamma_i)\delta(\Delta\Gamma_j), \quad (18)$$

where $\delta(\Delta\Gamma_i)$ denotes the change of the partial decay rate in the ith q^2 interval.

(d) *Tracking, PID, and γ, η, π^0 reconstruction*: The systematic uncertainties associated with the e^+ tracking and PID efficiencies, pion tracking and PID efficiencies, and γ, η, π^0 reconstruction are estimated by varying the corresponding correction factors for efficiencies within $\pm 1\sigma$. Using the new efficiency matrix, the element of the corresponding systematic covariance matrix is calculated by

$$C_{ij}^{\text{sys}}(\text{Tracking}, \text{PID}, \gamma/\eta/\pi^0 \text{rec}) = \delta(\Delta\Gamma_i)\delta(\Delta\Gamma_j), \quad (19)$$

where $\delta(\Delta\Gamma_i)$ denotes the change of the partial decay rate in the ith q^2 interval.

(e) *M_{miss}^2 fit*: The systematic covariance matrix arising from the uncertainty in the M_{miss}^2 fit has elements

$$C_{ij}^{\text{sys}}(M_{\text{miss}}^2 \text{fit}) = \left(\frac{1}{\tau_{D_s^+} N_{\text{tag}}}\right)^2 \sum_\alpha \varepsilon_{i\alpha}^{-1} \varepsilon_{j\alpha}^{-1} (\sigma_\alpha^{\text{fit}})^2, \quad (20)$$

where $\sigma_\alpha^{\text{fit}}$ is the systematic uncertainty of the number of signal events observed in the interval α obtained by varying the background shape in the M_{miss}^2 fit.

(f) *Remaining uncertainties*: The remaining uncertainties are assumed to be fully correlated across q^2 intervals and the element of the corresponding systematic covariance matrix is calculated by

$$C_{ij}^{\text{sys}} = \sigma(\Delta\Gamma_i)\sigma(\Delta\Gamma_j), \quad (21)$$

where $\sigma(\Delta\Gamma_i) = \sigma_{\text{sys}} \cdot \Delta\Gamma_i$ and σ_{sys} is the corresponding uncertainty reported in Table V.

Tables XI and XII give the systematic uncertainties for all sources in the different q^2 intervals, and Tables XIII and XIV give the elements of the systematic covariance density matrices for $D_s^+ \to \eta e^+ \nu_e$ and $D_s^+ \to \eta' e^+ \nu_e$, respectively.

D. Results based on individual fits

For each semileptonic decay, the product $f_+^{\eta^{(\prime)}}(0)|V_{cs}|$ and one of the parameters M_{pole}, α, or r_1 are determined by constructing and minimizing the χ^2 defined in Eq. (12). The covariance matrices used in these fits are shown in Tables XIII and XIV. Figure 5 shows individual fits to the differential decay rates of $D_s^+ \to \eta e^+ \nu_e$ and $D_s^+ \to \eta' e^+ \nu_e$ and (second row) the hadronic transition form factors as a function of q^2. The results obtained from individual fits are listed in Table XV.

E. Results based on simultaneous fits

Since the results for the hadronic transition form factors are consistent with each other, simultaneous fits to the differential decay rates of $D_s^+ \to \eta e^+ \nu_e$ and $D_s^+ \to \eta' e^+ \nu_e$ are performed to improve the statistical precision.

The values of $\Delta\Gamma_{\text{msr}}^i$ measured by the two $\eta^{(\prime)}$ sub-decays are fitted simultaneously, with results shown in Fig. 6. In the fits, the $\Delta\Gamma_{\text{msr}}^i$ becomes a vector of length $2m$ and C_{ij} becomes a $2m \times 2m$ covariance matrix. The uncorrelated and correlated systematic uncertainties are the same as shown in Table V.

For fully correlated systematic uncertainties, the matrices are constructed in the same way as done for the individual fits. For the uncorrelated systematic uncertainties, the matrix takes the form

$$C_{ij} = \begin{pmatrix} A & 0 \\ 0 & B \end{pmatrix},$$

where A and B are the matrices obtained from the individual decays. Table XVI summarizes the fit results obtained from the simultaneous, where the obtained values of $f_+^{\eta^{(\prime)}}(0)|V_{cs}|$ with different hadronic transition form factor parametrizations are consistent with each other.

Combining $|V_{cs}| = 0.97349 \pm 0.00016$ from the global fit in the standard model [13] with $f_+^{\eta^{(\prime)}}(0)|V_{cs}|$ extracted from the 2-Par series expansion, we determine

TABLE XI. Systematic uncertainties (in %) of the measured decay rates of $D_s^+ \to \eta e^+ \nu_e$ in various q^2 intervals.

	$D_s^+ \to \eta_{\gamma\gamma} e^+ \nu_e$								$D_s^+ \to \eta_{\pi^0\pi^+\pi^-} e^+ \nu_e$							
	1	2	3	4	5	6	7	8	1	2	3	4	5	6	7	8
ST D_s^- yields	0.50	0.50	0.50	0.50	0.50	0.50	0.50	0.50	0.50	0.50	0.50	0.50	0.50	0.50	0.50	0.50
D_s^+ lifetime	0.80	0.80	0.80	0.80	0.80	0.80	0.80	0.80	0.80	0.80	0.80	0.80	0.80	0.80	0.80	0.80
π^0/η reconstruction	1.84	1.59	1.32	1.08	0.96	0.90	0.89	0.87	0.94	1.00	1.06	1.16	1.27	1.37	1.59	1.90
$\pi^\pm$ tracking	...	...	...	...	...	...	...	...	0.95	1.01	1.09	1.17	1.27	1.38	1.51	1.74
$\pi^\pm$ PID	...	...	...	...	...	...	...	...	0.16	0.17	0.18	0.21	0.24	0.26	0.31	0.39
e^+ tracking	0.50	0.50	0.50	0.50	0.50	0.50	0.50	0.50	0.50	0.50	0.50	0.50	0.50	0.50	0.50	0.50
e^+ PID	0.08	0.09	0.09	0.10	0.11	0.10	0.12	0.12	0.06	0.08	0.09	0.11	0.09	0.12	0.11	0.11
Transition $\gamma(\pi^0)$ reconstruction	1.00	1.00	1.00	1.00	1.00	1.00	1.00	1.00	1.00	1.00	1.00	1.00	1.00	1.00	1.00	1.00
Smallest $|\Delta E|$	1.00	1.00	1.00	1.00	1.00	1.00	1.00	1.00	1.00	1.00	1.00	1.00	1.00	1.00	1.00	1.00
Peaking background	0.40	0.40	0.40	0.40	0.40	0.40	0.40	0.40	0.40	0.40	0.40	0.40	0.40	0.40	0.40	0.40
Hadronic transition form factors	0.17	1.29	2.22	0.85	0.07	0.81	0.79	0.19	0.27	0.93	5.06	4.21	6.96	1.56	1.84	8.22
$\eta_{\pi^0\pi^+\pi^-}$ selection	...	...	...	...	...	...	...	...	0.10	0.10	0.10	0.10	0.10	0.10	0.10	0.10
Tag bias	0.40	0.40	0.40	0.40	0.40	0.40	0.40	0.40	0.10	0.10	0.10	0.10	0.10	0.10	0.10	0.10
$E_{\mathrm{extra},\gamma}^{\max}$ and $N_{\mathrm{extra}}^{\mathrm{char}}$ requirements	0.70	0.70	0.70	0.70	0.70	0.70	0.70	0.70	2.00	2.00	2.00	2.00	2.00	2.00	2.00	2.00
M_{miss}^2 fit	0.10	0.37	0.24	0.48	0.69	3.05	0.85	0.38	0.40	0.11	0.38	0.57	2.01	1.35	1.89	4.00
MC statistics	0.92	1.14	1.26	1.35	1.51	1.65	1.80	1.49	1.14	1.37	1.46	1.74	2.06	2.09	2.42	2.19
Quoted branching fractions	0.50	0.50	0.50	0.50	0.50	0.50	0.50	0.50	1.10	1.10	1.10	1.10	1.10	1.10	1.10	1.10
Total	2.91	3.14	3.54	2.85	2.81	4.20	3.10	2.72	3.44	3.65	6.23	5.69	8.28	4.59	5.12	10.18

TABLE XII. Systematic uncertainties (%) of the measured decay rates of $D_s^+ \to \eta' e^+ \nu_e$ in various q^2 intervals.

	$D_s^+ \to \eta'_{\eta\pi^+\pi^-} e^+ \nu_e$			$D_s^+ \to \eta'_{\gamma\rho^0} e^+ \nu_e$		
	1	2	3	1	2	3
ST D_s^- yields	0.50	0.50	0.50	0.50	0.50	0.50
D_s^+ lifetime	0.80	0.80	0.80	0.80	0.80	0.80
π^0/η reconstruction	0.76	0.81	0.96	...	...	...
$\pi^\pm$ tracking	1.65	1.79	1.96	0.67	0.70	0.74
$\pi^\pm$ PID	0.35	0.40	0.47	0.11	0.09	0.08
e^+ tracking	0.50	0.50	0.50	0.50	0.50	0.50
e^+ PID	0.11	0.12	0.14	0.11	0.11	0.13
Transition $\gamma(\pi^0)$ reconstruction	1.00	1.00	1.00	1.00	1.00	1.00
Smallest $|\Delta E|$	1.00	1.00	1.00	1.00	1.00	1.00
Peaking background	1.00	1.00	1.00	1.00	1.00	1.00
Hadronic transition form factors	1.58	2.75	0.76	0.26	1.69	0.90
η' selection	0.10	0.10	0.10	1.40	1.40	1.40
Tag bias	0.10	0.10	0.10	0.10	0.10	0.10
χ^2 requirement	...	...	...	1.50	1.50	1.50
$E_{\mathrm{extra},\gamma}^{\max}$ and $N_{\mathrm{extra}}^{\mathrm{char}}$ requirements	2.00	2.00	2.00	1.10	1.10	1.10
M_{miss}^2 fit	0.52	0.50	1.27	0.30	0.75	9.18
MC statistics	0.35	0.48	0.72	0.71	0.91	1.38
Quoted branching fractions	1.30	1.30	1.30	1.40	1.40	1.40
Total	4.02	4.69	4.19	3.56	4.04	9.95

$f_+^\eta(0) = 0.4642 \pm 0.0073_{\mathrm{stat}} \pm 0.0066_{\mathrm{syst}}$ and $f_+^{\eta'}(0) = 0.540 \pm 0.025_{\mathrm{stat}} \pm 0.009_{\mathrm{syst}}$. Alternatively, we determine $|V_{cs}|$ with $D_s^+ \to \eta^{(\prime)} e^+ \nu_e$ decays by taking the $f_+^{\eta^{(\prime)}}(0)$ given by theoretical calculations. With $f_+^\eta(0) = 0.495_{-0.029}^{+0.030}$ and $f_+^{\eta'}(0) = 0.558_{-0.045}^{+0.047}$ from Ref. [4], we

obtain $|V_{cs}|_\eta = 0.913 \pm 0.014_{\mathrm{stat}} \pm 0.013_{\mathrm{syst}}{}_{-0.053\,\mathrm{theo}}^{+0.055}$ and $|V_{cs}|_{\eta'} = 0.941 \pm 0.044_{\mathrm{stat}} \pm 0.016_{\mathrm{syst}}{}_{-0.076\,\mathrm{theo}}^{+0.079}$, where the third uncertainties originate from the input FFs. These results agree with the measurements of $|V_{cs}|$ using $D \to \bar{K}\ell^+\nu_\ell$ [50–55] and $D_s^+ \to \ell^+\nu_\ell$ decays [56–60].

TABLE XIII. Statistical and systematic uncertainty density matrices for the measured partial decay rates of $D_s^+ \to \eta e^+ \nu_e$ in different q^2 intervals.

Statistical correlation matrix

ρ_{ij}^{stat}	$D_s^+ \to \eta_{\gamma\gamma} e^+ \nu_e$								$D_s^+ \to \eta_{\pi^0\pi^+\pi^-} e^+ \nu_e$							
	1	2	3	4	5	6	7	8	1	2	3	4	5	6	7	8
1	1.000	−0.187	0.019	−0.003	0.000	0.000	0.000	0.000	0.000	0.000	0.000	0.00	0.000	0.000	0.000	0.000
2		1.000	−0.236	0.025	−0.004	0.000	0.000	−0.001	0.000	0.000	0.000	0.000	0.000	0.000	0.000	0.000
3			1.000	−0.259	0.029	−0.005	0.000	0.000	0.000	0.000	0.000	0.000	0.000	0.000	0.000	0.000
4				1.000	−0.262	0.030	−0.006	−0.001	0.000	0.000	0.000	0.000	0.000	0.000	0.000	0.000
5					1.000	−0.259	0.029	−0.005	0.000	0.000	0.000	0.000	0.000	0.000	0.000	0.000
6						1.000	−0.247	0.017	0.000	0.000	0.000	0.000	0.000	0.000	0.000	0.000
7							1.000	−0.168	0.000	0.000	0.000	0.000	0.000	0.000	0.000	0.000
8								1.000	0.000	0.000	0.000	0.000	0.000	0.000	0.000	0.000
1									1.000	−0.174	0.012	−0.002	−0.001	0.000	−0.001	0.000
2										1.000	−0.212	0.011	−0.003	−0.001	−0.001	0.000
3											1.000	−0.223	0.012	−0.001	−0.001	−0.001
4												1.000	−0.234	0.012	−0.005	−0.001
5													1.000	−0.230	0.016	−0.003
6														1.000	−0.231	0.008
7															1.000	−0.180
8																1.000

Systematic correlation matrix

ρ_{ij}^{syst}	$D_s^+ \to \eta_{\gamma\gamma} e^+ \nu_e$								$D_s^+ \to \eta_{\pi^0\pi^+\pi^-} e^+ \nu_e$							
	1	2	3	4	5	6	7	8	1	2	3	4	5	6	7	8
1	1.000	0.738	0.609	0.734	0.738	0.468	0.672	0.730	0.497	0.469	0.243	0.371	0.184	0.417	0.397	0.277
2		1.000	0.790	0.805	0.673	0.270	0.486	0.673	0.476	0.532	0.590	−0.016	0.551	0.522	0.511	−0.134
3			1.000	0.701	0.578	0.256	0.337	0.610	0.422	0.518	0.724	−0.225	0.698	0.530	0.523	−0.345
4				1.000	0.633	0.262	0.548	0.683	0.463	0.497	0.493	0.061	0.448	0.468	0.451	−0.055
5					1.000	0.234	0.652	0.674	0.437	0.422	0.267	0.259	0.214	0.368	0.345	0.161
6						1.000	0.230	0.458	0.272	0.225	0.006	0.325	−0.035	0.170	0.151	0.274
7							1.000	0.536	0.368	0.306	0.012	0.436	−0.043	0.232	0.206	0.365
8								1.000	0.446	0.438	0.306	0.228	0.254	0.385	0.362	0.124
1									1.000	0.829	0.565	0.495	0.472	0.767	0.712	0.313
2										1.000	0.660	0.340	0.584	0.763	0.721	0.129
3											1.000	−0.302	0.917	0.699	0.686	−0.437
4												1.000	−0.376	0.215	0.185	0.853
5													1.000	0.644	0.688	−0.426
6														1.000	0.715	0.117
7															1.000	0.110
8																1.000

VIII. SUMMARY

Analyzing 7.33 fb⁻¹ $e^+ e^-$ collision data taken at center-of-mass energies between 4.128 GeV and 4.226 GeV with the BESIII detector, the absolute branching fractions of $D_s^+ \to \eta e^+ \nu_e$ and $D_s^+ \to \eta' e^+ \nu_e$ are measured. Compared to Ref. [23], which used a subset of the dataset of the present analysis, the precision of the branching fractions of $D_s^+ \to \eta e^+ \nu_e$ and $D_s^+ \to \eta' e^+ \nu_e$ is improved by a factor of 1.3 and 1.7, respectively, and the precision of $f_+^{\eta'}(0)|V_{cs}|$ is improved by a factor of 2.2. The precision of $f_+^{\eta}(0)|V_{cs}|$ is

not improved because the uncertainty in the previous paper [23] is underestimated by a factor of two due to incorrect construction of the χ^2 in the fits to the partial decay rates (see [61] for details). For simple comparison, we also present the results based on 3.19 fb⁻¹ of data at $E_{CM} = 4.178$ GeV in the Appendix. After fixing this issue, the precision of $f_+^{\eta}(0)|V_{cs}|$ is improved by a factor of 1.4 as expected.

Combining the new branching fractions with those of $D^+ \to \eta e^+ \nu_e$ and $D^+ \to \eta' e^+ \nu_e$ measured by BESIII [62], the $\eta - \eta'$ mixing angle $\phi_P = (40.0 \pm 2.0_{stat} \pm 0.6_{syst})°$ is
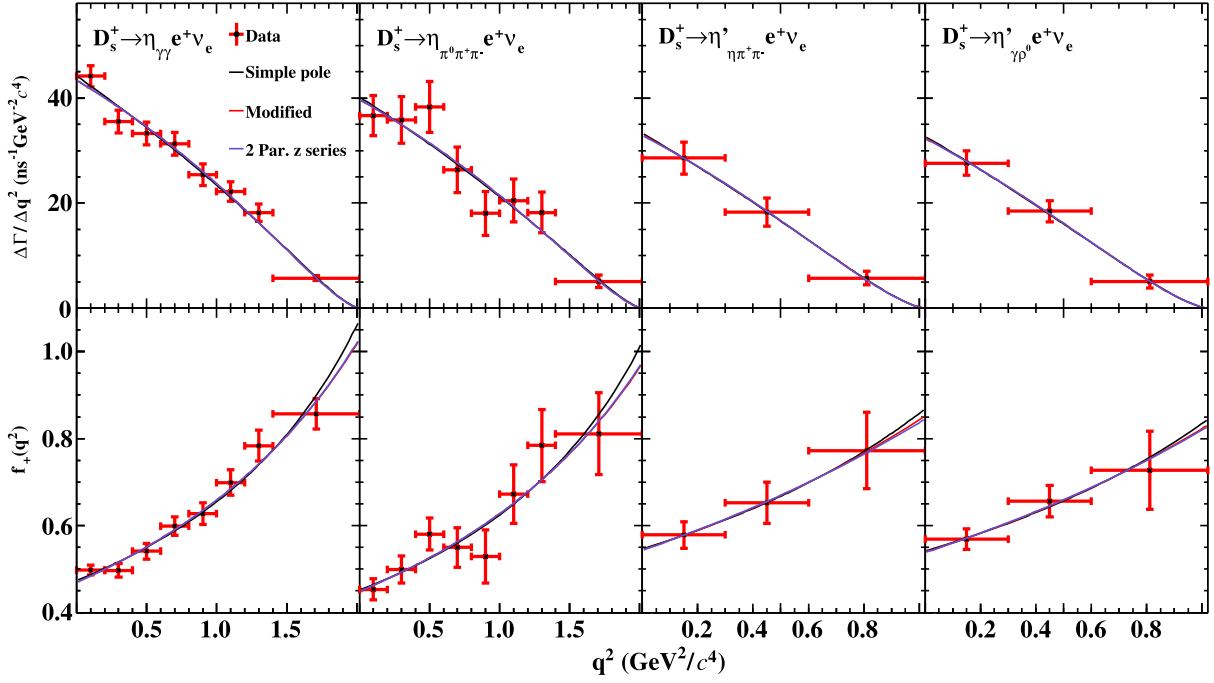
FIG. 5.　Top row: Individual fits to the differential decay rates of $D_s^+ \to \eta e^+ \nu_e$ and $D_s^+ \to \eta' e^+ \nu_e$ and (bottom row). Projections on the hadronic transition form factors as a function of q^2. The points with error bars are (top row) the measured differential decay rates and (bottom row) the hadronic transition form factors. The black, red, and blue curves are the form factors parameterized by simple pole model, modified pole model, and 2-Par series expansion, respectively.

TABLE XIV.　Statistical and systematic uncertainty density matrices for the measured partial decay rates of $D_s^+ \to \eta' e^+ \nu_e$ in different q^2 intervals.

Statistical correlation matrix					
$D_s^+ \to \eta'_{\eta\pi^+\pi^-} e^+ \nu_e$			$D_s^+ \to \eta'_{\gamma\rho^0} e^+ \nu_e$		
ρ_{ij}^{stat} 　1	2	3	1	2	3
1　1.000	−0.123	0.009	0.000	0.000	0.000
2	1.000	−0.124	0.000	0.000	0.000
3		1.000	0.000	0.000	0.000
1			1.000	−0.104	0.003
2				1.000	−0.110
3					1.000

Systematic correlation matrix					
$D_s^+ \to \eta'_{\eta\pi^+\pi^-} e^+ \nu_e$			$D_s^+ \to \eta'_{\gamma\rho^0} e^+ \nu_e$		
ρ_{ij}^{syst} 　1	2	3	1	2	3
1　1.000	0.508	0.924	0.348	0.121	0.080
2	1.000	0.648	0.236	0.492	0.153
3		1.000	0.332	0.204	0.098
1			1.000	0.818	0.311
2				1.000	0.258
3					1.000
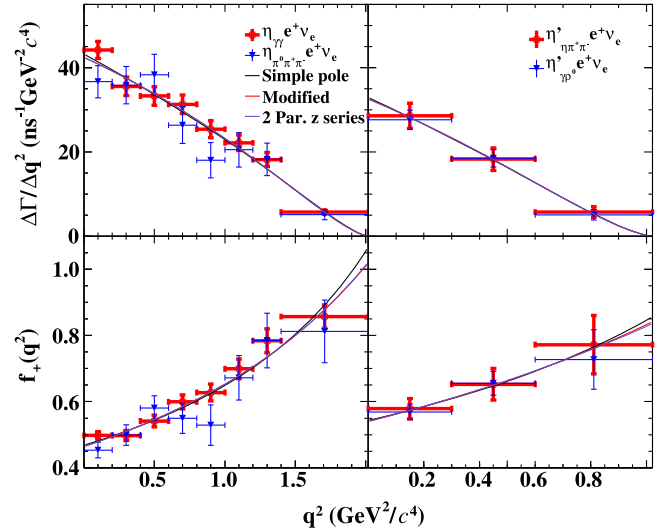
FIG. 6.　Top row: simultaneous fits to the differential decay rates of (left) $D_s^+ \to \eta_{\gamma\gamma} e^+ \nu_e$ and $D_s^+ \to \eta_{\pi^0\pi^+\pi^-} e^+ \nu_e$ and (right) $D_s^+ \to \eta'_{\eta\pi^+\pi^-} e^+ \nu_e$ and $D_s^+ \to \eta'_{\rho^0\gamma} e^+ \nu_e$, and (bottom row) the hadronic transition form factors as function of q^2. The red circles and blue triangles with error bars are (top row) the measured differential decay rates for two $\eta^{(\prime)}$ channels and (bottom row). Projections on the hadronic transition form factors. The black, red, and blue curves are the form factors parameterized by simple pole model, modified pole model, and 2-Par series expansion, respectively.

TABLE XV.   The parameters obtained from individual fits to the partial decay rates of $D_s^+ \to \eta e^+ \nu_e$ or $D_s^+ \to \eta' e^+ \nu_e$. The first and second uncertainties are statistical and systematic, respectively. $N_{\text{d.o.f.}}$ is the number of degrees of freedom.

	Simple pole			Modified pole			Series 2-Par		
Decay	$f_+^{\eta^{(\prime)}}(0)\|V_{cs}\|$	M_{pole}	$\chi^2/N_{\text{d.o.f.}}$	$f_+^{\eta^{(\prime)}}(0)\|V_{cs}\|$	α	$\chi^2/N_{\text{d.o.f.}}$	$f_+^{\eta^{(\prime)}}(0)\|V_{cs}\|$	r_1	$\chi^2/N_{\text{d.o.f.}}$
$\eta_{\gamma\gamma}e^+\nu_e$	0.4613(67)(65)	1.90(04)(02)	5.3/6	0.4568(75)(67)	0.37(09)(03)	4.9/6	0.4570(78)(68)	−2.59(45)(15)	4.9/6
$\eta_{\pi^0\pi^+\pi^-}e^+\nu_e$	0.440(15)(08)	1.90(11)(03)	5.0/6	0.437(16)(08)	0.35(21)(06)	5.0/6	0.437(17)(08)	−2.5(11)(03)	5.0/6
$\eta'_{\eta\pi^+\pi^-}e^+\nu_e$	0.532(34)(10)	1.66(31)(04)	0.0/1	0.530(36)(10)	0.75(75)(10)	0.0/1	0.529(39)(11)	−6.5(60)(09)	0.0/1
$\eta'_{\gamma\rho^0}e^+\nu_e$	0.527(28)(10)	1.69(30)(07)	0.2/1	0.525(29)(11)	0.69(66)(18)	0.2/1	0.524(31)(11)	−6.1(53)(14)	0.1/1

TABLE XVI.   The parameters obtained from simultaneous fits to the partial decay rates of $D_s^+ \to \eta e^+ \nu_e$ or $D_s^+ \to \eta' e^+ \nu_e$. The first and second uncertainties are statistical and systematic, respectively. $N_{\text{d.o.f.}}$ is the number of degrees of freedom.

	Simple pole			Modified pole			Series 2-Par		
Decay	$f_+^{\eta^{(\prime)}}(0)\|V_{cs}\|$	M_{pole}	$\chi^2/N_{\text{d.o.f.}}$	$f_+^{\eta^{(\prime)}}(0)\|V_{cs}\|$	α	$\chi^2/N_{\text{d.o.f.}}$	$f_+^{\eta^{(\prime)}}(0)\|V_{cs}\|$	r_1	$\chi^2/N_{\text{d.o.f.}}$
$\eta e^+\nu_e$	0.4559(61)(63)	1.90(04)(01)	13.3/14	0.4517(68)(64)	0.37(08)(03)	12.8/14	0.4519(71)(65)	−2.63(41)(14)	12.8/14
$\eta' e^+\nu_e$	0.529(21)(09)	1.67(22)(04)	0.3/4	0.527(23)(09)	0.73(50)(12)	0.2/4	0.525(24)(09)	−6.3(40)(10)	0.2/4

extracted, providing information related to the gluon component in the η' meson. By analyzing the partial decay rates of $D_s^+ \to \eta e^+ \nu_e$ and $D_s^+ \to \eta' e^+ \nu_e$, the products of $f_+^{\eta^{(\prime)}}(0)|V_{cs}|$ are determined. Furthermore, taking the value of $|V_{cs}|$ from a standard model fit (CKMfitter, [13]) as input, the form factors at zero momentum transfer squared $f_+^{\eta^{(\prime)}}(0)$ are determined. The measured hadronic transition form factors provide important pieces of information to test the various theoretical calculations [2,4–6,9,11,12]. Figure 7 shows the comparisons of the $f_+^{\eta^{(\prime)}}(0)$ obtained in this paper and different theoretical predictions. Alternatively, we determine $|V_{cs}|$ with the $D_s^+ \to \eta^{(\prime)} e^+ \nu_e$ decays by taking the $f_+^{\eta^{(\prime)}}(0)$ given by theoretical calculations [4]. These results on $|V_{cs}|$ together with those measured by $D \to \bar{K}\ell^+\nu_\ell$ and $D_s^+ \to \ell^+\nu_\ell$ are important to test the unitarity of the CKM matrix. The branching fractions, hadronic

transition form factors and $|V_{cs}|$ reported in this work supersede the corresponding results in Ref. [23], based on the 3.19 fb^{-1} subset of data at $E_{\text{CM}} = 4.178$ GeV.
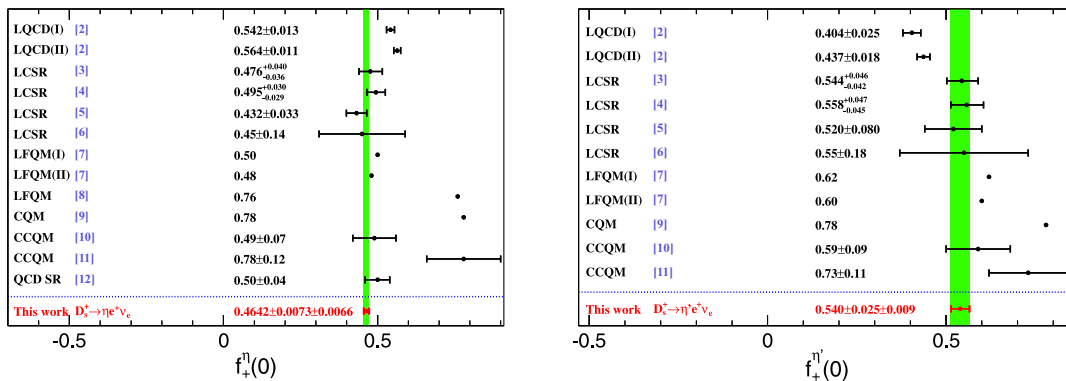
FIG. 7.   Comparisons of the form factors $f_+^{\eta^{(\prime)}}(0)$ measured by this work with the theoretical calculations. The first and second uncertainties are statistical and systematic, respectively. The green bands correspond to the $\pm 1\sigma$ limits of the form factors measured by this work. For the predictions by LQCD, no systematic uncertainties have been considered.

APPENDIX: THE RESULTS WITH DATA TAKEN AT $E_{\mathrm{CM}} = 4.178$ GeV

Figure 8 shows the results of the fits to the M_{miss}^2 distributions of the candidate events for $D_s^+ \to \eta e^+ \nu_e$ and $D_s^+ \to \eta' e^+ \nu_e$, based on the 3.19 fb^{-1} of $e^+ e^-$ collision

TABLE XVII. Signal efficiencies ($\epsilon_{\gamma(\pi^0)\mathrm{SL}}$), signal yields ($N_{\mathrm{DT}}$), and obtained branching fractions ($\mathcal{B}_{\mathrm{SL}}$) for various semi-electronic decays based on the data sample taken at $E_{\mathrm{CM}} = 4.178$ GeV. Efficiencies do not include the branching fractions of $\eta^{(\prime)}$ subdecays. Numbers in the first and second parentheses are the statistical and systematic uncertainties, respectively.

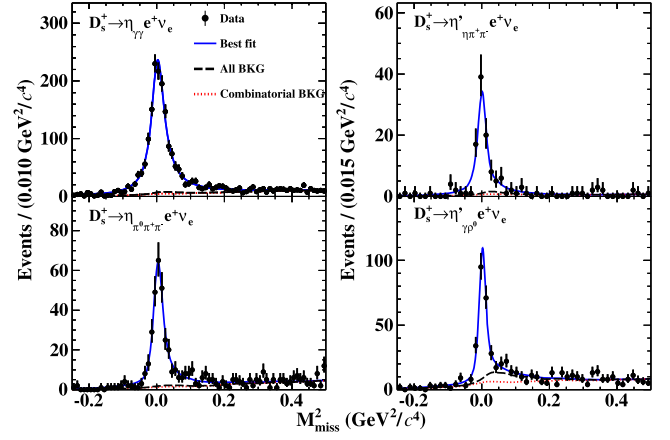| Decay	$\eta^{(\prime)}$ decays	$\epsilon_{\gamma(\pi^0)\mathrm{SL}}$ (%)	N_{DT}	$\mathcal{B}_{\mathrm{SL}}$ (%)
$\eta e^+ \nu_e$	$\gamma\gamma$	46.35(11)	2010(49)	2.257(55)(51)
	$\pi^0 \pi^+ \pi^-$	17.33(09)		
$\eta' e^+ \nu_e$	$\eta\pi^+\pi^-$	19.68(07)	337(22)	0.804(53)(22)
	$\gamma\rho^0$	24.26(10)		

FIG. 8. Fits to the M_{miss}^2 distributions of the candidate events for various semileptonic decays from data taken at $E_{\mathrm{CM}} = 4.178$ GeV. The points with error bars represent data. The blue solid curves denote the total fits, and the red solid dotted curves show the fitted combinatorial background contributions. Differences between dashed and dotted curves are due to the backgrounds from $D_s^+ \to \eta^{(\prime)} \pi^+ \pi^0$, $\eta^{(\prime)} \mu^+ \nu_\mu$, and $D_s^+ \to \phi(1020)_{\pi^0 \pi^+ \pi^-} e^+ \nu_e$.

data taken at $E_{\mathrm{CM}} = 4.178$ GeV. The obtained signal yields, signal efficiencies and branching fractions are summarized in Table XVII.

Figure 9 shows the simultaneous fits to the partial decay rates of $D_s^+ \to \eta e^+ \nu_e$ or $D_s^+ \to \eta' e^+ \nu_e$ reconstructed with
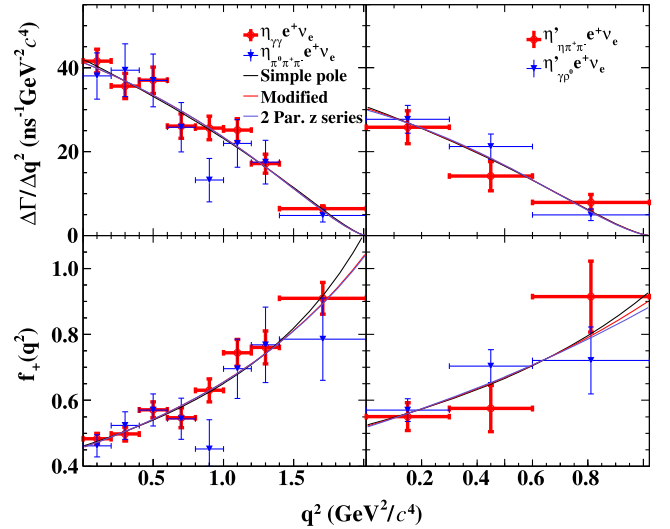

FIG. 9. Top row: simultaneous fits to the differential decay rates of (left) $D_s^+ \to \eta_{\gamma\gamma} e^+ \nu_e$ and $D_s^+ \to \eta_{\pi^0 \pi^+ \pi^-} e^+ \nu_e$ and (right) $D_s^+ \to \eta'_{\eta\pi^+\pi^-} e^+ \nu_e$ and $D_s^+ \to \eta'_{\rho^0\gamma} e^+ \nu_e$, and (bottom row) the hadronic transition form factors as function of q^2 for the data sample taken at $E_{\mathrm{CM}} = 4.178$ GeV. The red circles and blue triangles with error bars are (top row) the measured differential decay rates for two $\eta^{(\prime)}$ channels and (bottom row). Projections on the hadronic transition form factors. The black, red, and blue curves are the form factors parameterized by simple pole model, modified pole model, and 2-Par series expansion, respectively.

TABLE XVIII. The parameters obtained from simultaneous fits to the partial decay rates of $D_s^+ \to \eta e^+ \nu_e$ or $D_s^+ \to \eta' e^+ \nu_e$ for the data sample taken at $E_{CM} = 4.178$ GeV. Numbers in the first and second parentheses are the statistical and systematic uncertainties, respectively. $N_{d.o.f.}$ is the number of degrees of freedom.

	Simple pole			Modified pole			Series 2-Par		
Decay	$f_+^{\eta^{(\prime)}}(0)\|V_{cs}\|$	M_{pole}	$\chi^2/N_{d.o.f.}$	$f_+^{\eta^{(\prime)}}(0)\|V_{cs}\|$	α	$\chi^2/N_{d.o.f.}$	$f_+^{\eta^{(\prime)}}(0)\|V_{cs}\|$	r_1	$\chi^2/N_{d.o.f.}$
$\eta e^+ \nu_e$	0.4494(085)(067)	1.85(05)(02)	13.6/14	0.4452(095)(068)	0.45(11)(04)	13.9/14	0.4454(101)(068)	−2.99(58)(18)	13.9/14
$\eta' e^+ \nu_e$	0.511(28)(08)	1.53(19)(02)	3.8/4	0.507(30)(08)	1.10(59)(07)	3.8/4	0.504(34)(09)	−9.3(50)(06)	3.8/4

two different decay modes and the hadronic transition form factors as function of q^2. The parameters obtained for the hadronic transition form factors are summarized in Table XVIII.

Tables XIX and XX summarize the q^2 ranges, the fitted numbers of observed events (N_{DT}), the numbers of generated events (N_{prd}) calculated by the weighted efficiency matrices and the decay rates ($\Delta\Gamma$) of $D_s^+ \to \eta e^+ \nu_e$ and $D_s^+ \to \eta' e^+ \nu_e$ in various q^2 intervals, respectively.

Tables XXI and XXII show the statistical and systematic uncertainty covariance density matrices for $D_s^+ \to \eta e^+ \nu_e$ and $D_s^+ \to \eta' e^+ \nu_e$, respectively.

TABLE XIX. The partial decay rates of $D_s^+ \to \eta e^+ \nu_e$ in various q^2 intervals of data for the data sample taken at $E_{CM} = 4.178$ GeV. Numbers in the parentheses are the statistical uncertainties.

i q^2 (GeV^2/c^4)		1 (m_e^2, 0.2)	2 (0.2, 0.4)	3 (0.4, 0.6)	4 (0.6, 0.8)	5 (0.8, 1.0)	6 (1.0, 1.2)	7 (1.2, 1.4)	8 (1.4, 2.02)
$D_s^+ \to \eta_{\gamma\gamma} e^+ \nu_e$	N_{DT}^i	320(19)	274(18)	264(18)	199(16)	185(15)	173(14)	122(12)	142(14)
	N_{prd}^i	1682(113)	1441(122)	1497(127)	1055(117)	1037(114)	1016(110)	692(091)	797(085)
	$\Delta\Gamma_{msr}^i$ (ns^{-1})	8.32(56)	7.13(61)	7.40(63)	5.21(58)	5.12(56)	5.02(54)	3.42(45)	3.94(42)
$D_s^+ \to \eta_{\pi^0\pi^+\pi^-} e^+ \nu_e$	N_{DT}^i	70(09)	68(09)	59(08)	40(07)	23(06)	29(06)	23(05)	20(05)
	N_{prd}^i	1538(222)	1594(255)	1495(256)	1044(238)	534(210)	888(229)	707(210)	594(189)
	$\Delta\Gamma_{msr}^i$ (ns^{-1})	7.60(110)	7.88(126)	7.39(126)	5.16(118)	2.64(104)	4.39(113)	3.49(104)	2.94(093)

TABLE XX. The partial decay rates of $D_s^+ \to \eta' e^+ \nu_e$ in various q^2 intervals of data for the data sample taken at $E_{CM} = 4.178$ GeV. Numbers in the parentheses are the statistical uncertainties.

i q^2 (GeV^2/c^4)		1 (m_e^2, 0.3)	2 (0.3, 0.6)	3 (0.6, 1.02)
$D_s^+ \to \eta'_{\eta_{\gamma\gamma}\pi^+\pi^-} e^+ \nu_e$	N_{DT}^i	52(08)	29(06)	21(05)
	N_{prd}^i	1566(238)	858(210)	673(159)
	$\Delta\Gamma_{msr}^i$ (ns^{-1})	7.7(12)	4.2(10)	3.3(08)
$D_s^+ \to \eta'_{\gamma\rho^0} e^+ \nu_e$	N_{DT}^i	120(14)	90(12)	32(08)
	N_{prd}^i	1680(202)	1285(182)	418(118)
	$\Delta\Gamma_{msr}^i$ (ns^{-1})	8.3(10)	6.4(09)	2.1(06)

TABLE XXI. Statistical and systematic uncertainty density matrices for the measured partial decay rates of $D_s^+ \to \eta e^+ \nu_e$ in different q^2 intervals.

Statistical correlation matrix

$\rho_{ij}^{\mathrm{stat}}$	$D_s^+ \to \eta_{\gamma\gamma} e^+ \nu_e$								$D_s^+ \to \eta_{\pi^0\pi^+\pi^-} e^+ \nu_e$							
	1	2	3	4	5	6	7	8	1	2	3	4	5	6	7	8
1	1.000	−0.181	0.017	−0.003	−0.001	0.000	−0.001	0.000	0.000	0.000	0.000	0.00	0.000	0.000	0.000	0.000
2		1.000	−0.232	0.025	−0.004	0.000	0.000	−0.002	0.000	0.000	0.000	0.000	0.000	0.000	0.000	0.000
3			1.000	−0.248	0.024	−0.005	0.000	0.000	0.000	0.000	0.000	0.000	0.000	0.000	0.000	0.000
4				1.000	−0.252	0.026	−0.005	−0.001	0.000	0.000	0.000	0.000	0.000	0.000	0.000	0.000
5					1.000	−0.247	0.027	−0.005	0.000	0.000	0.000	0.000	0.000	0.000	0.000	0.000
6						1.000	−0.239	0.012	0.000	0.000	0.000	0.000	0.000	0.000	0.000	0.000
7							1.000	−0.159	0.000	0.000	0.000	0.000	0.000	0.000	0.000	0.000
8								1.000	0.000	0.000	0.000	0.000	0.000	0.000	0.000	0.000
1									1.000	−0.167	0.011	−0.001	0.000	−0.001	0.000	0.000
2										1.000	−0.207	0.007	−0.004	−0.001	−0.001	0.000
3											1.000	−0.208	0.010	0.001	−0.001	−0.001
4												1.000	−0.225	0.008	−0.003	0.000
5													1.000	−0.226	0.016	−0.002
6														1.000	−0.231	0.008
7															1.000	−0.183
8																1.000

Systematic correlation matrix

$\rho_{ij}^{\mathrm{syst}}$	$D_s^+ \to \eta_{\gamma\gamma} e^+ \nu_e$								$D_s^+ \to \eta_{\pi^0\pi^+\pi^-} e^+ \nu_e$							
	1	2	3	4	5	6	7	8	1	2	3	4	5	6	7	8
1	1.000	0.504	−0.024	0.461	0.715	0.834	0.777	0.821	0.376	0.374	−0.189	0.618	−0.243	0.323	−0.123	0.551
2		1.000	0.769	0.621	0.709	0.520	0.207	0.182	0.546	0.534	0.633	−0.158	0.593	0.580	0.607	−0.324
3			1.000	0.412	0.358	0.060	−0.288	−0.362	0.406	0.393	0.905	−0.622	0.893	0.486	0.827	−0.778
4				1.000	0.429	0.551	0.520	0.307	0.359	0.351	0.305	0.020	0.273	0.357	0.297	−0.083
5					1.000	0.656	0.479	0.573	0.480	0.470	0.215	0.248	0.162	0.446	0.225	0.123
6						1.000	0.713	0.755	0.381	0.374	−0.099	0.506	−0.153	0.313	−0.059	0.425
7							1.000	0.802	0.197	0.196	−0.412	0.677	−0.456	0.110	−0.347	0.661
8								1.000	0.206	0.205	−0.473	0.757	−0.521	0.109	−0.400	0.743
1									1.000	0.903	0.568	0.318	0.497	0.884	0.604	0.064
2										1.000	0.544	0.313	0.475	0.870	0.588	0.073
3											1.000	−0.552	0.959	0.629	0.913	−0.746
4												1.000	−0.589	0.200	−0.408	0.939
5													1.000	0.558	0.942	−0.755
6														1.000	0.651	−0.039
7															1.000	−0.597
8																1.000

TABLE XXII. Statistical and systematic uncertainty density matrices for the measured partial decay rates of $D_s^+ \to \eta' e^+ \nu_e$ in different q^2 intervals.

	Statistical correlation matrix					
	$D_s^+ \to \eta'_{\eta\pi^+\pi^-} e^+ \nu_e$			$D_s^+ \to \eta'_{\gamma\rho^0} e^+ \nu_e$		
ρ_{ij}^{stat}	1	2	3	1	2	3
1	1.000	−0.119	0.008	0.000	0.000	0.000
2		1.000	−0.124	0.000	0.000	0.000
3			1.000	0.000	0.000	0.000
1				1.000	−0.103	0.003
2					1.000	−0.102
3						1.000
	Systematic correlation matrix					
	$D_s^+ \to \eta'_{\eta\pi^+\pi^-} e^+ \nu_e$			$D_s^+ \to \eta'_{\gamma\rho^0} e^+ \nu_e$		
ρ_{ij}^{syst}	1	2	3	1	2	3
1	1.000	0.678	0.822	0.222	0.354	0.280
2		1.000	0.946	0.485	0.134	0.093
3			1.000	0.429	0.226	0.170
1				1.000	0.692	0.549
2					1.000	0.744
3						1.000

[1] B. C. Ke, J. Koponen, H. B. Li, and Y. H. Zheng, Annu. Rev. Nucl. Part. Sci. **73**, 285 (2023).

[2] G. S. Bali, S. Collins, S. Dürr, and I. Kanamori, Phys. Rev. D **91**, 014503 (2015).

[3] D. D. Hu, H. B. Fu, T. Zhong, L. Zeng, W. Cheng, and X. G. Wu, Eur. Phys. J. C **82**, 12 (2022).

[4] G. Duplančić and B. Melic, J. High Energy Phys. 11 (2015) 138.

[5] N. Offen, F. A. Porkert, and A. Schäfer, Phys. Rev. D **88**, 034023 (2013).

[6] K. Azizi, R. Khosravi, and F. Falahati, J. Phys. G **38**, 095001 (2011).

[7] Z. T. Wei, H. W. Ke, and X. F. Yang, Phys. Rev. D **80**, 015022 (2009).

[8] R. C. Verma, J. Phys. G **39**, 025005 (2012).

[9] D. Melikhov and B. Stech, Phys. Rev. D **62**, 014006 (2000).

[10] M. A. Ivanov, J. G. Körner, J. N. Pandya, P. Santorelli, N. R. Soni, and C. T. Tran, Front. Phys. (Beijing) **14**, 64401 (2019).

[11] N. R. Soni, M. A. Ivanov, J. G. Körner, J. N. Pandya, P. Santorelli, and C. T. Tran, Phys. Rev. D **98**, 114031 (2018).

[12] P. Colangelo and F. De Fazio, Phys. Lett. B **520**, 78 (2001).

[13] R. L. Workman et al. (Particle Data Group), Prog. Theor. Exp. Phys. **2022**, 083C01 (2022).

[14] C. Di Donato, G. Ricciardi, and I. I. Bigi, Phys. Rev. D **85**, 013016 (2012).

[15] M. Ablikim et al. (BES Collaboration), Phys. Rev. D **73**, 052008 (2006).

[16] R. Aaij et al. (LHCb Collaboration), J. High Energy Phys. 01 (2015) 024.

[17] N. H. Christ, C. Dawson, T. Izubuchi, C. Jung, Q. Liu, R. D. Mawhinney, C. T. Sachrajda, A. Soni, and R. Zhou, Phys. Rev. Lett. **105**, 241601 (2010).

[18] J. J. Dudek, R. G. Edwards, B. Joo, M. J. Peardon, D. G. Richards, and C. E. Thomas, Phys. Rev. D **83**, 111502 (2011).

[19] G. Brandenburg et al. (CLEO Collaboration), Phys. Rev. Lett. **75**, 3804 (1995).

[20] J. Yelton et al. (CLEO Collaboration), Phys. Rev. D **80**, 052007 (2009).

[21] J. Hietala, D. Cronin-Hennessy, T. Pedlar, and I. Shipsey, Phys. Rev. D **92**, 012009 (2015).

[22] M. Ablikim et al. (BESIII Collaboration), Phys. Rev. D **94**, 112003 (2016).

[23] M. Ablikim et al. (BESIII Collaboration), Phys. Rev. Lett. **122**, 121801 (2019).

[24] M. Ablikim et al. (BESIII Collaboration), Chin. Phys. C **39**, 093001 (2015); **46**, 113002 (2022). These articles described the integrated luminosity measurement for data taken at $\sqrt{s} = 4.189$, 4.199, 4.209, 4.219, and 4.226 GeV. The integrated luminosity values for the other data samples have been obtained by a similar procedure.

[25] M. Ablikim *et al.* (BESIII Collaboration), Nucl. Instrum. Methods Phys. Res., Sect. A **614**, 345 (2010).

[26] C. H. Yu *et al.*, in Proceedings of IPAC2016, Busan, Korea (2016), 10.18429/JACoW-IPAC2016-TUYA01.

[27] M. Ablikim *et al.* (BESIII Collaboration), Chin. Phys. C **44**, 040001 (2020).

[28] H. B. Li and X. R. Lyu, Natl. Sci. Rev. **8**, nwab181 (2021).

[29] X. Li *et al.*, Radiat. Detect. Technol. Methods **1**, 13 (2017); Y. X. Guo *et al.*, Radiat. Detect. Technol. Methods **1**, 15 (2017); P. Cao *et al.*, Nucl. Instrum. Methods Phys. Res., Sect. A **953**, 163053 (2020).

[30] S. Agostinelli *et al.* (GEANT4 Collaboration), Nucl. Instrum. Methods Phys. Res., Sect. A **506**, 250 (2003).

[31] K. X. Huang, Z. J. Li, Z. Qian, J. Zhu, H. Y. Li, Y. M. Zhang, S. S. Sun, and Z. Y. You, Nucl. Sci. Tech. **33**, 142 (2022).

[32] S. Jadach, B. F. L. Ward, and Z. Was, Phys. Rev. D **63**, 113009 (2001); Comput. Phys. Commun. **130**, 260 (2000).

[33] M. Ablikim *et al.* (BESIII Collaboration), Measurement of the cross section for $e^+e^- \to D_s^\pm D_s^{*\mp}$ up to 4.7 GeV (to be published).

[34] R. G. Ping, Chin. Phys. C **38**, 083001 (2014).

[35] D. J. Lange, Nucl. Instrum. Methods Phys. Res., Sect. A **462**, 152 (2001); R. G. Ping, Chin. Phys. C **32**, 599 (2008).

[36] C. Patrignani, Chin. Phys. C **40**, 100001 (2016).

[37] J. C. Chen, G. S. Huang, X. R. Qi, D. H. Zhang, and Y. S. Zhu, Phys. Rev. D **62**, 034003 (2000); R. L. Yang, R. G. Ping, and H. Chen, Chin. Phys. Lett. **31**, 061301 (2014).

[38] E. Richter-Was, Phys. Lett. B **303**, 163 (1993).

[39] R. M. Baltrusaitis *et al.* (MARK III Collaboration), Phys. Rev. Lett. **56**, 2140 (1986); J. Adler *et al.* (MARK III Collaboration), Phys. Rev. Lett. **60**, 89 (1989).

[40] M. Ablikim *et al.* (BESIII Collaboration), Phys. Rev. D **104**, 052009 (2021).

[41] M. Ablikim *et al.* (BESIII Collaboration), Phys. Rev. Lett. **122**, 071802 (2019).

[42] M. Ablikim *et al.* (BESIII Collaboration), Phys. Rev. D **99**, 072002 (2019).

[43] X. Ma, Z. P. Mao, J. M. Bian *et al.*, Chin. Phys. C **32**, 744 (2008).

[44] M. Schmelling, Phys. Scr. **51**, 676 (1995).

[45] M. Ablikim *et al.* (BESIII Collaboration), Phys. Rev. D **83**, 112005 (2011).

[46] T. Becher and R. J. Hill, Phys. Lett. B **633**, 61 (2006).

[47] D. Becirevic and A. B. Kaidalov, Phys. Lett. B **478**, 417 (2000).

[48] C. G. Boyd, B. Grinstein, and R. F. Lebed, Nucl. Phys. **B461**, 493 (1996).

[49] M. Lefebvre, R. K. Keeler, R. Sobie, and J. White, Nucl. Instrum. Methods Phys. Res., Sect. A **451**, 520 (2000).

[50] M. Ablikim *et al.* (BESIII Collaboration), Phys. Rev. D **92**, 072012 (2015).

[51] M. Ablikim *et al.* (BESIII Collaboration), Phys. Rev. D **92**, 112008 (2015).

[52] M. Ablikim *et al.* (BESIII Collaboration), Phys. Rev. Lett. **122**, 011804 (2019).

[53] D. Besson *et al.* (CLEO Collaboration), Phys. Rev. D **80**, 032005 (2009).

[54] B. Aubert *et al.* (*BABAR* Collaboration), Phys. Rev. D **76**, 052005 (2007).

[55] L. Widhalm *et al.* (Belle Collaboration), Phys. Rev. Lett. **97**, 061804 (2006).

[56] M. Ablikim *et al.* (BESIII Collaboration), Phys. Rev. D **94**, 072004 (2016).

[57] A. Zupanc *et al.* (Belle Collaboration), J. High Energy Phys. 09 (2013) 139.

[58] P. del Amo Sanchez *et al.* (*BABAR* Collaboration), Phys. Rev. D **82**, 091103 (2010); **91**, 019901(E) (2015).

[59] P. U. E. Onyisi *et al.* (CLEO Collaboration), Phys. Rev. D **79**, 052002 (2009).

[60] P. Naik *et al.* (CLEO Collaboration), Phys. Rev. D **80**, 112004 (2009).

[61] In Ref. [23], the χ^2 is constructed to be $\chi^2 = \sum_{ij}(\Delta\Gamma_i^{\rm msr} - \Delta\Gamma_i^{\rm th})C_{ij}^{-1}(\Delta\Gamma_j^{\rm msr} - \Delta\Gamma_j^{\rm th})/\sigma(\Delta\Gamma_i^{\rm msr})/\sigma(\Delta\Gamma_j^{\rm msr})$, where there is an additional term of $\sigma(\Delta\Gamma_i^{\rm msr})\sigma(\Delta\Gamma_j^{\rm msr})$ used for test but not removed when obtaining nominal results. This mistake only changes $f_+^\eta(0)|V_{cs}|$ by 0.2%, but underestimates its uncertainty by a factor of 2.

[62] M. Ablikim *et al.* (BESIII Collaboration), Phys. Rev. D **97**, 092009 (2018).